Square spiral photonic crystals: Robust architecture for microfabrication of materials with large three-dimensional photonic band gaps

Ovidiu Toader and Sajeev John
Department of Physics, University of Toronto, 60 St. George Street, Toronto, Ontario, Canada M5S-1A7
(Received 12 February 2002; published 26 July 2002)

We provide a blueprint for microfabricating photonic crystals with very large and robust three-dimensional photonic band gaps (PBG's). These crystals are based on interleaving polygonal spiral posts and can be efficiently manufactured on a large scale in a one-step process using the recently introduced technique of glancing angle deposition. We classify various families of spiral photonic crystals based on (i) the parent three-dimensional (3D) point lattice to which they are most closely related, (ii) the crystallographic axis of the parent lattice around which the spiral posts wind, and (iii) the set of points of the parent lattice which the spiral arms connect or nearly connect. We obtain optimal geometries for the spiral photonic crystals by detailed mapping of the size and location of the PBG within a multidimensional parameter space which characterizes the shape of each spiral post. For the optimum PBG, the spiral arms and elbows may deviate significantly from the points of the original point lattice. The largest 3D PBG's are obtained for square spiral posts that wind around the [001] axis of diamond (or face centered cubic) lattice and in which the spiral arm segments approximately connect either the fifth or first nearest-neighbor points of the parent lattice. In the case of silicon posts (with a dielectric constant of 11.9) in an air background, whose arm segments nearly connect fifth nearest-neighbor point of the diamond lattice, the full PBG can be as large as 16% of the gap center frequency. For the corresponding air posts in a silicon background, the maximum PBG is 24% of the gap center frequency. We compute both the total electromagnetic density of states and the electromagnetic field distributions near the PBG. It is suggested the PBG in an optimized structure is highly tolerant to various forms of disorder that may arise during the manufacturing process.

DOI: 10.1103/PhysRevE.66.016610 PACS number(s): 42.70.Qs

I. INTRODUCTION

Photonic band gap (PBG) [1–3] materials are artificial dielectric crystals with a spatial periodicity on the optical wavelength scale. The geometry of the crystal's building blocks facilitate a synergetic interplay between certain macroscopic (Bragg) and microscopic light scattering resonances leading to a spectral region where the electromagnetic waves are forbidden from propagating inside the crystal. The ability to trap or localize light [4] makes the PBG material a versatile platform for integrated optics on a microscopic scale in which a variety of passive and active microphotonic devices and optical microcircuitry [5] can be incorporated. Unlike integrated optics based on refractive index guiding, microcircuitry based on light localization is highly robust to perturbations that could scatter light out of the microcircuit. In addition, light localization provides robust, microscopic control over spontaneous emission from light emitters in active devices placed within the PBG material.

Large scale microfabrication of three-dimensional (3D) photonic crystals with band gaps centered at a wavelength shorter than 2 μm has been a major materials science challenge over the past decade. An equally great challenge has been the design of a photonic crystal structure with a large 3D PBG which at the same time is amenable to efficient, large scale manufacturing. While initial theoretical studies focused on structures related to the face centered cubic (FCC) lattice [1,2], it was soon realized that creation of a complete PBG near the lowest-order Bragg scattering resonance would require a nonspherical basis in the unit cell. The diamond lattice, which contains two lattice points within each FCC unit cell, satisfies this requirement and has since been considered the ''ideal'' structure for a large 3D PBG. This was demonstrated by band structure calculations [6] that showed that a diamond lattice of overlapping spheres both in a low and high index of refraction background produces a large and complete 3D PBG. Moreover, a tetrahedral network of cylindrical bonds connecting all of the nearest-neighbor points of the diamond lattice [7] exhibits the largest complete PBG of any computed structure for a single material of given refractive index in an air background. However, the synthesis of diamond structures with features on the micron scale [8] has, so far, been impractical. This has led to a shift of attention to other prototype structures that capture essential features of the diamond network.

The first microfabricated diamondlike structures involved the drilling of a periodic array of criss-crossing pores in a high refractive index semiconductor [8]. Visual inspection reveals that this structure is remarkably similar to a diamond lattice of highly overlapping air spheres in a solid matrix. Criss-crossing pores are straightforward to implement on the microwave length scale. However, the drilling of holes on the micron scale, to more than a few microns depth by reactive ion etching has proved impractical. Recently, photoelectrochemical etching methods [9,10] have allowed very deep etches of criss-crossing pores in silicon and various III–V semiconductors. However, disorder effects are difficult to control at the junction points where pores cross each other. Approaches based on exfoliation of material using focused ion beams [11] yield high-quality structures but are expensive and require tedious drilling of individual holes.

The second microfabricated diamondlike PBG material is the ''woodpile'' structure [12,13]. This requires complex and time-consuming microlithography. In the case of silicon based woodpile structures [14], this lithography entails layer by layer fabrication, repetitious etching, chemical vapor deposition, and surface polishing. The result is a PBG material consisting of approximately two-photonic crystal unit cells in the vertical direction, made of polycrystalline silicon and a complete 3D PBG of nearly 20% of the gap center at 1.6 μm [15]. In the case of GaAs and InP woodpile structures [16], a dry-etching method is used on single-crystal semiconductor. After a large planar area of the initial layer is fabricated, the sample is cut and folded onto itself, thereby doubling the number of layers in the vertical direction. The folded segments are aligned by laser diffraction methods and then bonded together. Through this complex procedure, up to three unit cells (12 layers) of photonic crystal have been grown in the vertical direction.

In view of the intricate semiconductor photolithography required in the approaches described above, it is useful to explore alternative self-assembly methods. Sometimes referred to as ''soft lithography'' [17] these methods generally make use of a photonic crystal template that can be grown with relative ease. For example, careful sedimentation of monodisperse SiO_2 (glass) spheres in a suitable viscous solution leads to very high-quality ''artificial opals'' consisting of a close packed FCC lattice. This template consists of roughly 74% glass by volume and 26% interstitial air pockets. After a small amount of heat treatment (sintering) to create small necks (where the spheres touch), the template is placed within a chemical vapor deposition chamber and infiltrated with silicon. This silicon uniformly ''wets'' the surface of the glass balls and fills 90–97 % of the air voids in the optimal structure. Indeed, it has been shown that nearly epitaxial growth of silicon can be achieved within the complex geometry of the opal template [18]. When the original glass template is removed by selective chemical etching, what remains is an ''inverse opal'' [18–20] with a complete PBG spanning roughly 5–9 % of the center frequency. Unlike the PBG of the diamond structure, the PBG of the FCC inverse opal is relatively unstable to disorder effects. On the other hand, a template consisting of a close-packed diamond lattice of silica spheres has not yet been realized since the solid volume filling fraction (in this case 34%) is very small compared to that which occurs using standard sphere sedimentation techniques.

The four major categories of 3D PBG materials, which have been studied previously, can be classified according to the frequency bands between which a full photonic band gap appears. The number of frequency bands below the full PBG depends on the size of the unit cell in which the periodic structure is defined. For example, a lattice with a given unit cell can be alternatively described by a larger unit cell that has twice the volume of the original. In the second (equivalent) description, the number of bands that appears below the full photonic band gap would be double the number of bands that appears below the full PBG in the original description and each of the bands in the second description would contain half the number of electromagnetic modes when compared to the bands in the original description. Accordingly, we exclude categories that arise purely from such changes in the definition of the unit cell and in what follows we use the smallest possible unit cell for a given photonic crystal structure.

In the first category are photonic crystals that exhibit a complete PBG between the eighth and ninth bands of the photonic band structure. This includes the Bravais lattices of spheres such as the face centered cubic lattice, the hexagonal close packed (HCP) lattice, the body centered cubic (BCC) lattice, and minor variations of these structures. These PBG materials generally exhibit a small (less than 10%) PBG between the eighth and ninth bands but are accompanied by large pseudogaps (a frequency range in which the photon density of states is strongly suppressed but does not vanish) between lower bands. This category entails the widely studied inverse opal structures discussed above. In the second category are PBG materials that exhibit a complete gap between the second and third bands (sometimes referred to as the fundamental gap) of the photonic band structure. This includes the diamond lattice of spheres, the inverse diamond lattice, the tetrahedral network of rods on a diamond lattice, the criss-crossing pore structure, and the woodpile structure discussed above. PBG materials in this category generally have very large gaps (20–28%) and the gap is highly robust to disorder effects. In the third category are PBG materials that exhibit a complete gap between the fifth and sixth bands of the photonic band structure. These include simple cubic mesh structures [21]. All structures in category 3, which have been studied so far, exhibit relatively small (less than 10%) photonic band gaps. The square spiral photonic crystals that we present in this paper belong to a fourth category, namely, PBG materials that exhibit a complete gap between the fourth and fifth bands of the photonic band structure.

The photonic band structure for certain circular spiral post structures was discussed previously by Chutinan and Noda [22]. These circular spiral posts may be arrayed in either a body centered cubic, face centered cubic, or simple cubic (SC) lattice structure. The FCC and BCC structures are based on visual similarity to the diamond lattice. In both of these structures, the spiral rods are arranged in a lattice but adjacent spiral rods are mutually half period shifted as the rods wind in the vertical direction. These structures are predicted to have a PBG between the second and third bands. Chutinan and Noda describe a particular set of geometrical parameters for which the FCC circular spiral photonic crystal exhibits a PBG that is comparable in size to the diamond network. However, microfabrication of the FCC circular spiral structure has so far been impractical. Deposition methods such as glancing angle deposition (GLAD) [23] cannot be readily applied to this structure due to the half period shift between adjacent spiral rods. Another method involves three-dimensional lithography using a two-photon confocal microscope [24]. The corresponding PBG for the BCC circular spirals is smaller than that of the FCC circular spirals. The simple cubic circular spiral structure is distinct from either the FCC or BCC circular spiral structures. In the SC circular spiral, the adjacent spiral rods are not half period shifted from each other and the PBG appears between the fourth and

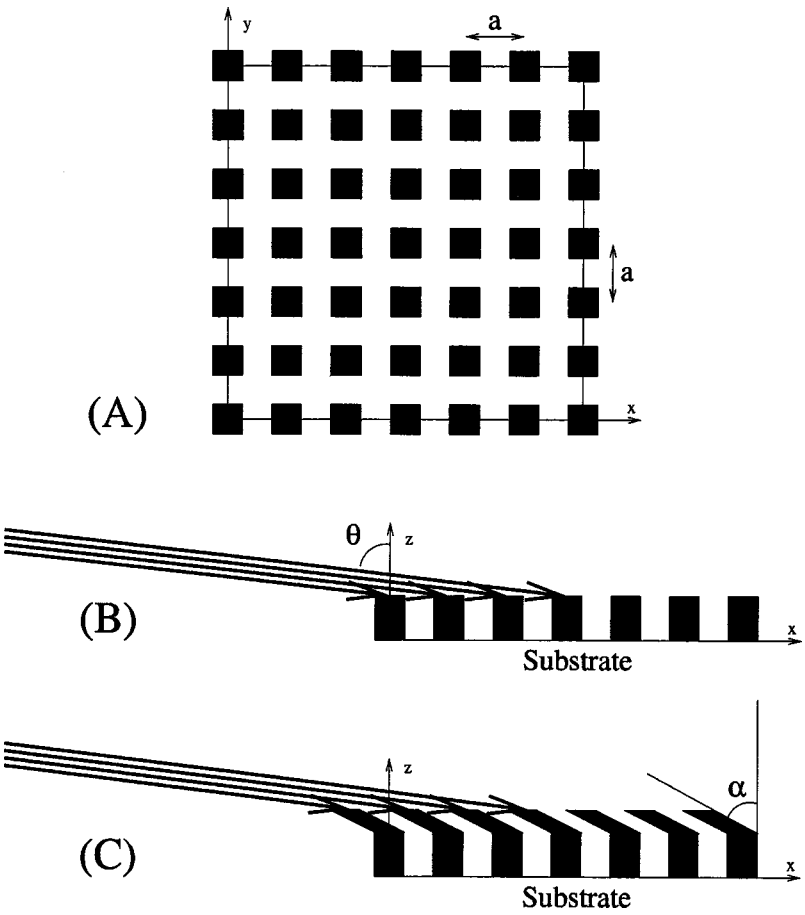

FIG. 1. GLAD requires the preparation of a lattice of seed posts on a suitable substrate (a). A vapor is deposited at an oblique angle θ (b) leading to the growth of posts in a predetermined direction characterized by the growth angle α (c). The substrate is placed on a computer controlled turntable that allows independent rotations about (i) an axis that is normal to the substrate and (ii) a second axis that lies along the surface of the substrate.

fifth bands. Chutinan and Noda obtained a 16.8% PBG in a SC circular spiral structure in which the background material has a dielectric constant of 12.25 and the rods consist of air. A variant of the circular spiral structures involving woven dielectric fibers has been discussed by Tsai *et al.* [25]. However, the maximum gaps in this study are no larger than 7%.

In this paper we present an alternative photonic crystal architecture that realizes the benefits of a diamondlike structure without the disadvantages of tedious and expensive microlithography. In the optimum case, this new 3D PBG material consists of a two-dimensional (2D) array of interleaving square spiral posts on a tetragonal lattice. These structures do not involve a phase shift between adjacent spirals and are ideally suited for efficient manufacturing using the GLAD technique. We report a complete 3D PBG as large as 24% of the gap center frequency when the material is made of silicon (dielectric constant 11.9). This gap is comparable in magnitude with the largest PBG (28%) predicted in an optimized tetrahedral bonding network of the same dielectric constant.

In Sec. II we briefly describe the GLAD method, which can be used to microfabricate this type of crystal with a micron scale lattice constant on a very large semiconductor wafer. Section III introduces the several new families of PBG materials together with a suitable nomenclature to identify them. In Sec. IV the spiral crystals with a very large PBG, belonging to the [001]-diamond:*n* family (the nomenclature introduced in Sec. III), are studied in detail. In Sec. V we study square spiral structures with a large PBG belonging to the [001]-FCC:*n* family. These photonic crystals are based on a face centered cubic lattice and exhibit a PBG of up to 17% of the midgap frequency when comprised of silicon and air. Section VI discusses in detail the relationship between the square spiral crystals and previously studied diamondlike photonic crystals.

II. GLANCING ANGLE DEPOSITION METHOD

GLAD is a relatively new thin-film deposition technique that allows 3D control of film structures on the nanometer scale. The technique [23,26] is based on physical vapor deposition in a vacuum chamber. The process starts by forming a regular pattern of short seed posts on a flat substrate. These seed posts are features on the surface of the substrate and can be created by conventional electron beam lithography or photolithography [see Fig. 1(a)]. A collimated vapor flux is then directed at a large incident angle θ [see Fig. 1(b)] at the patterned substrate. At these large angles ($\theta > 70°$) only the seeds are visible to the incoming vapor flux. Self-shadowing (caused by orientation of the substrate relative to the vapor flux) combined with limited adatom surface diffusion leads to nucleation and growth almost exclusively on the top surface of the seed posts and to the emergence of oriented pillars extruded from the seed posts. These isolated pillars of deposited material grow towards the source of the vapor flux at a growth angle α [see Fig. 1(c)] that is smaller

than the incidence angle θ. α can be varied easily between 0° and a maximum angle whose value is determined by θ and the set of deposition conditions. If controlled substrate motion is combined with the vapor deposition then a variety of 3D microstructures can be fabricated. For example, helical posts can be created by rotating the substrate at a uniform rate and thereby continuously changing the growth direction. Similarly, nonuniform rotation of the substrate in the form of controlled 90° sudden ''jumps'' can lead to polygonal spiral posts with straight arms and sharp elbows. The porosity of the deposited material varies with the incidence angle θ and for a given material, it decreases with increasing θ. Also, the roughness of the microstructures depends on both the deposition conditions and the type of material being used. Simple materials that can be deposited using the GLAD technique include SiO_2, silicon, germanium, and MgF_2. A preliminary demonstration of the growth of a silicon based, tetragonal, square spiral, photonic crystal has been presented elsewhere [27]. Modification of the growth conditions during the GLAD process can also be used to vary the cross-sectional area of the spiral arms as a function of the vertical distance from the substrate. A particularly important application of this is in the growth of a ''capping layer'' once the spiral posts have reached a desired height [26]. This is accomplished by suddenly increasing the spiral arm thickness such that they merge into a solid slab at a given height. An alternative approach is to fill the square spiral crystal with a suitable photoresist, deposit a solid slab, and then remove the underlying photoresist. Following the growth of the capping layer, it is feasible to apply a further tetragonal distortion to the underlying square spiral crystal, if required by the theoretical blueprint, by simple mechanical compression [28]. After the solid slab is grown to a desired thickness, the top surface of the slab may be used as secondary substrate onto which a new spiral photonic crystal can be grown. The sandwiched slab acts as two-dimensional defect (planar waveguide) in between the 3D PBG materials above and below the slab. Patterning of the capping layer itself with a periodic two-dimensional array of holes as well as various line defects and point defects can also be implemented prior to growth of the second spiral PBG material on top of the capping slab.

Finally, we point out that structures described above can be used as templates for building ''inverted'' structures. For instance, a template made of SiO_2 can be infiltrated with high refractive index materials such as silicon, germanium, and possibly some III–V semiconductors. As in the case of ''inverse opals,'' the ''inversion'' process consists of filling all (or nearly all) of the air regions of the silica based photonic crystal with the higher index semiconductor and then selectively etching out the original silica spiral posts. Inverse spiral photonic crystals of this nature typically exhibit larger PBG's than their counterparts consisting of solid spiral posts.

III. DEFINITION OF POLYGONAL SPIRAL PHOTONIC CRYSTALS

PBG materials based on spiral posts can be classified into various families based on the underlying parent lattice from which they are derived and the algorithm used to generate them. The spiral arms and elbows in the optimized photonic crystal may, however, deviate significantly from the points of the parent lattice. The algorithm consists of (i) choosing a 3D Bravais or non-Bravais lattice, (ii) cutting this 3D lattice with an oriented 2D plane that intersects a periodic (2D) array of lattice points of the 3D lattice, (iii) placing seed posts on a substrate whose surface coincides with the 2D array of lattice points, (iv) extruding from the seed posts an array of spiral posts whose arms connect specified points of the 3D lattice, and (v) varying the position of the spiral arms and their elbows in the local vicinity of the 3D lattice points until an optimum PBG is obtained. In many cases, the ''elbow'' points of the optimized spiral posts may differ considerably from the points of the parent lattice. The orientation of the 2D plane is defined by a crystallographic axis vector $[\mathbf{m_1 m_2 m_3}]$ of the parent 3D lattice which is normal to the 2D plane. This axis is identified with the z axis of the spiral photonic crystal and the spiral posts grown by the GLAD method wind around this axis. The arms of the spiral posts are initially chosen to connect the points of the 3D lattice and the turning points (elbows) of the spiral are chosen initially to coincide with points of the 3D lattice. For a given 3D parent lattice and axis $[\mathbf{m_1 m_2 m_3}]$, there are distinct families of spiral posts defined by the particular points of the parent lattice which are joined by the arms of the spiral. A type n spiral is defined with arms that, in a straight line path, connect nth nearest-neighbor points of the 3D lattice. At the endpoint of each arm, the spiral segment forms an elbow to another segment that causes the post to wind around the z axis and connect the endpoint to its nth nearest-neighbor point on the 3D lattice. In what follows we show that type 5 spirals exhibit the largest PBG followed by class 1 spirals. The spiral structure within a given family is further defined by three parameters: L, the projection of the spiral arm length (distance between a pair of elbows) onto the plane of the substrate, c, the length along the z axis of the repeating (unit) cell, and r, the radius of the circular cross section of the arm. In cases where the cross section of the spiral arm is noncircular, the parameter r, is replaced with alternative descriptive parameter(s). For a given family of spirals, the set of parameters (L,c,r), for which a complete 3D PBG exists, defines an ''island'' within the larger set of spirals spanned by all L, c, and r. This ''island'' in parameter space may include spirals whose elbows occur precisely on the points of said three-dimensional lattice as well as ''distorted'' spirals obtained by various compressions or elongations of the spiral arms in which the elbows do not occur on the points of the 3D parent lattice. Typically, the optimum PBG occurs for a set (L,c,r) with considerable deviation from the underlying 3D parent lattice. In this paper, the label $[\mathbf{m_1 m_2 m_3}]$-3D lattice:n spiral is used to denote the family of spiral photonic crystals whose z axis is given by the $[\mathbf{m_1 m_2 m_3}]$ crystallographic axis of a specified ''3D lattice,'' whose spiral arm segments approximately connect nth nearest-neighbor points of the 3D lattice, and for which the refractive index of the spiral arms is greater than that of the background. We use the label inverse-$[\mathbf{m_1 m_2 m_3}]$-3D lattice:n to denote the corresponding crystal

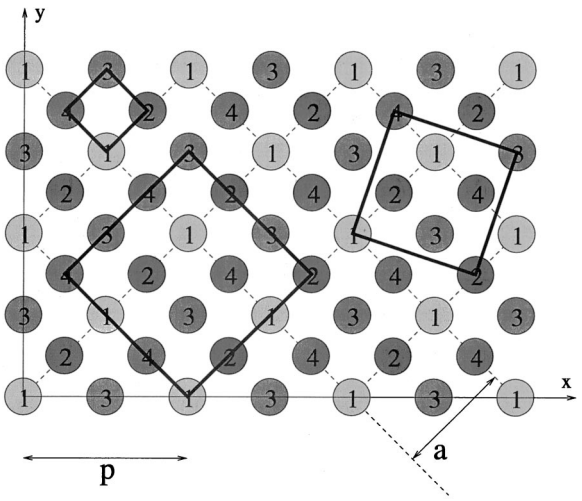

FIG. 2. Three [001]-diamond:*n* examples. *p* is the lattice constant of the conventional (FCC) unit cell and *a* is the lattice constant of the square lattice formed by the seeds on the substrate (dashed lines). The index on the points indicate the [001] plane on which the point lies, points with larger plane index occurring further above the $z=0$ plane. Top left spiral is a [001]-diamond:1 type, right spiral is a [001]-diamond:3 type and the center spiral is a [001]-diamond:5 type.

in which the spiral arms have a lower refractive index than the background.

We consider first the diamond lattice (see Fig. 2) which can be visualized as the union of two interpenetrating FCC lattices displaced from each other by a vector $[p/4,p/4,p/4]$ where p is the lattice constant of the conventional (FCC) unit cell. By intersecting the diamond lattice with four [001] planes placed, respectively, at $z=0,p/4,p/2,3p/4$ we obtain the arrangement depicted in Fig. 2 where the numerical label on each point represents the [001] plane on which the point lies; circles with larger numbers being placed on planes further above the $z=0$ plane. The next [001] layer of points (which would be labeled as 5) would be placed at $z=p$ and would fall right on top of layer 1 in Fig. 2. The type 1 points are arranged on a square lattice (dashed lines in Fig. 2) with lattice constant $a=p/\sqrt{2}$ which is rotated by 45° relative to the x and y axes. The number of points on each of the [001] layers described above is the same. Therefore the points on layer 1 can be placed in a one to one correspondence with the points on layer 2 and the same holds true for the points on higher layers. Various square spiral structures can be obtained by joining points on consecutive layers 1-2-3-4-5-,..., as described above. Three examples are shown in Fig. 2. We call the square spiral depicted in the top left part of the figure as being of type 1 because the arms of the spiral join nearest-neighbor points of the original diamond lattice. Similarly, the spiral depicted on the right is called type 3 and the spiral depicted in the lower center part is called type 5. If layer 1 corresponds to the seeds on the GLAD substrate, then by simultaneously growing identical spirals on this substrate one would join all the points of the diamond lattice. The spiral described above are denoted as [001]-diamond:*n* where $n=1$, 3, or 5.

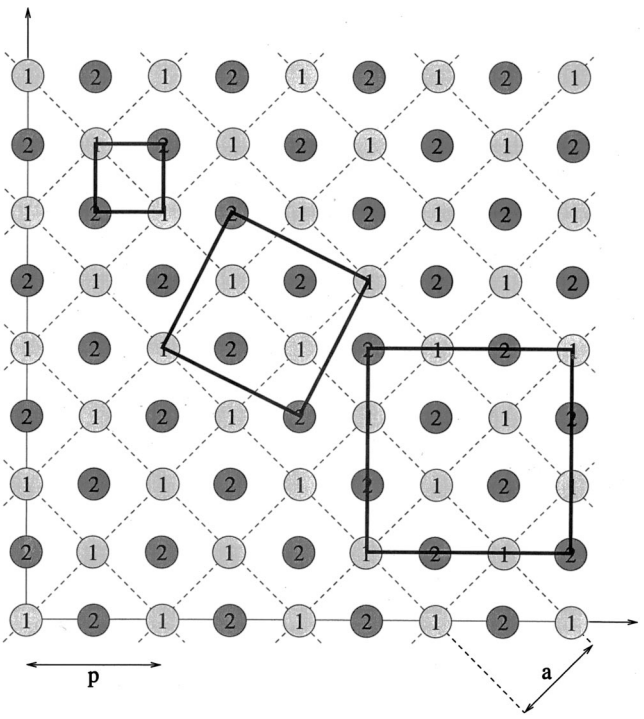

FIG. 3. Three [001]-FCC:*n* examples. *p* is the lattice constant of the conventional (FCC) unit cell and *a* is the lattice constant of the square lattice formed by the seeds on the substrate (dashed lines). The index on the points indicate the [001] plane on which the point lies. These square spirals are different from the ones depicted in Fig. 2. For example the type 1 and 5 spirals in this case are rotated by 45° relative to the substrate.

A similar procedure can be used to create a spiral photonic crystal based on a face centered cubic lattice. For the FCC lattice the construction analogous to Fig. 2 is illustrated in Fig. 3. In this case there are only two types of [001] planes with the next [001] layer (labeled as 3) falling directly on top of plane 1 and plane 4 falling directly on top of plane 2. A top view of the spiral arms associated with the families denoted by [001]-FCC:1, [001]-FCC:3, and [001]-FCC:5 is illustrated in Fig. 3. The substrate, in this case, is identical with the one discussed previously but the orientation of the square spirals relative to the lattice of seed posts is rotated by 45°. As in the case of diamond, the spiral arms join points on consecutive layers 1-2-3-4-5-,..., with 90° elbows formed at the transition from one plane to the next.

For both the diamond and FCC lattices one could replace the [001] ''substrate'' plane with another crystallographic plane (here we do not differentiate between equivalent crystallographic planes such as [001] or [100]). Following the algorithm described above one could identify new families of polygonal spirals whose elbows will be in a one to one correspondence with the points of the parent lattice. For example the [111]-FCC:*n* will lead to a crystal built from triangular spirals on a triangular substrate. In our study we find that the [001] spirals of the FCC and diamond lattices yield the largest photonic band gaps.

We note finally that our classification scheme does not differentiate between parent lattices that are deformed along

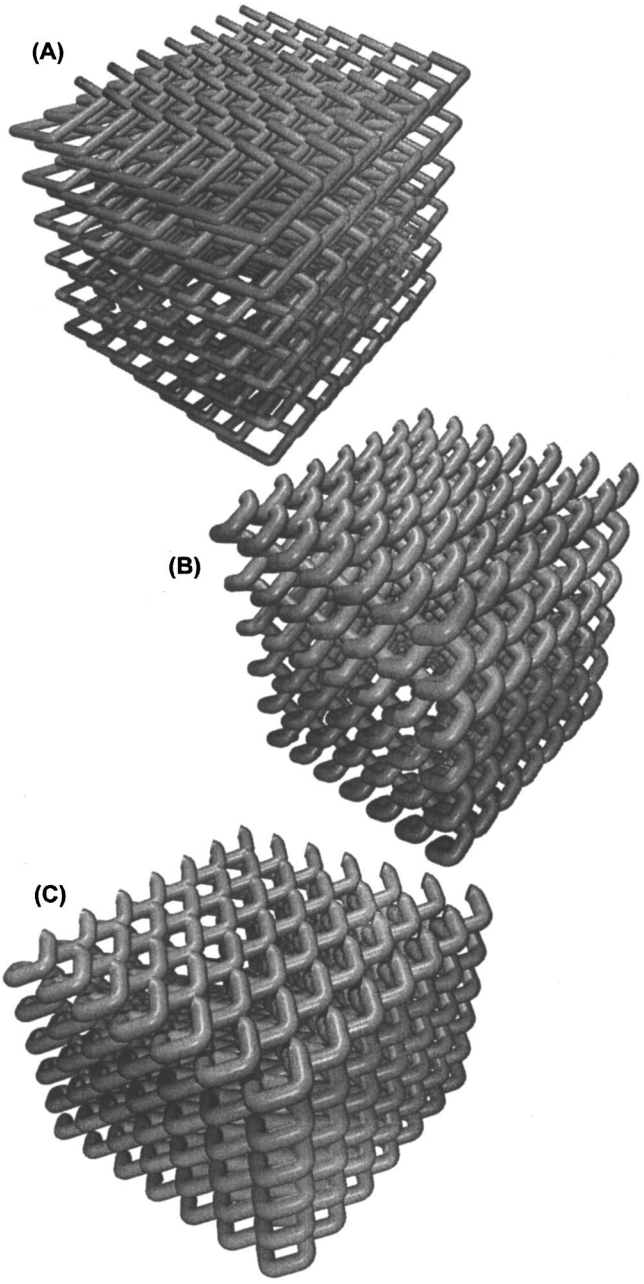

FIG. 4. Three illustrations of the square spirals crystals. (a) Optimized [001]-diamond:5 crystal. (b) Optimized [001]-diamond:1 crystal. (c) Optimized [001]-FCC:1 crystal. The building blocks of these crystals are described in Fig. 5. Each of the crystal fragments shown contains 7×7 spirals and all spirals have six complete turns.

the direction perpendicular to the selected plane. For example, Fig. 3 is valid for the tetragonal face centered lattice as well. Indeed in many cases that we describe below, the optimum spiral structure within a given family involves a considerable tetragonal distortion away from either the pure FCC or diamond lattices. The parent lattice is used only for reference and classification. The exact spiral structure within a given family is described by the exact shape of the spiral's skeleton and the arm cross section.

Figure 4 shows three examples of square spiral photonic crystals with circular cross section arms. Figure 4(a) is an illustration of a [001]-diamond:5 photonic crystal. Figure 4(b) shows a [001]-diamond:1 photonic crystal and Fig. 4(c) shows a [001]-FCC:1 photonic crystal.

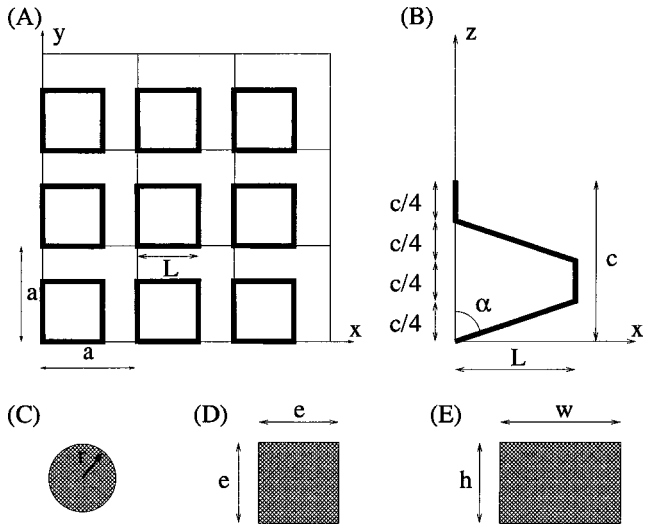

FIG. 5. Building blocks for [001]-diamond:n ($n=1,5$) type crystals. The substrate is a square lattice of lattice constant a [see (a)]. Viewed along the z axis the skeleton of the square spiral is a square of length L [see (a) and (b)]. The view along the y axis is shown in (b). c is the pitch of the square spiral and α is the growth angle [see Fig. 1(c)]. (c), (d), and (e) describe the circular, square, and rectangular arm cross section respectively.

IV. [001]-DIAMOND:*n* STRUCTURES

In this section we analyze in detail the family of [001]-diamond:n spiral photonic crystals and the corresponding inverse structures. Figure 4(a) shows a piece of the optimized (to be defined later) [001]-diamond:5 with circular cross-section arms. Similarly, in Fig. 4(b) is shown a piece of the optimized [001]-diamond:1.

The [001]-diamond:n crystals are described theoretically as a square spiral basis placed on a tetragonal lattice. The tetragonal crystal has lattice constant a along the x and y directions [the same a as the one shown in Fig. 1(a)] and c along the z direction. The basis of the crystal is a square spiral of pitch c [see Fig. 5(b)]. The pitch is the same as the lattice constant in the z direction and the spiral is wrapped around the z axis. The projection of the spiral's skeleton on the xy plane is a square with edge of length L [see Fig. 5(a)]. For the $n=1$ and $n=5$ crystals the projection of the spiral arms onto the xy plane lies parallel to the x or y axis, whereas in the [001]-diamond:3 crystal the spiral is rotated by an angle arctan (1/2) relative to the substrate (see Fig. 2). The GLAD growth angle for these crystals is $\alpha=90°-\arctan(c/4L)$. The cross section of the spiral's arm can be arbitrary. In this paper we restrict our attention to spirals having arms with circular, square or rectangular cross sections whose geometries are described in Figs. 5(c), 5(d), and 5(e), respectively.

The dielectric constant of the spiral is ϵ_{sp} and the spirals are embedded in a material whose dielectric constant is ϵ_b. In the following we will choose our unit of length to be a.

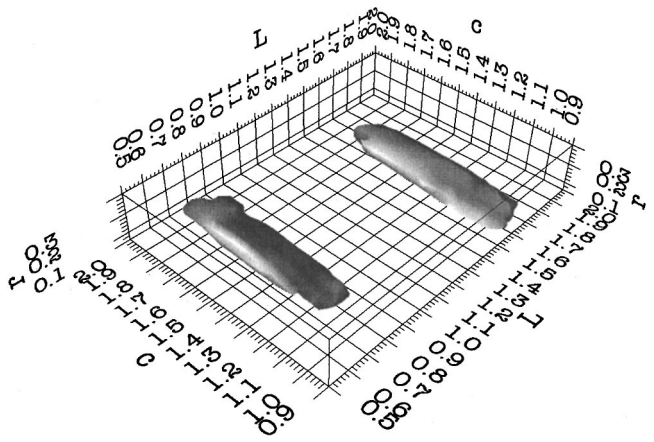

FIG. 6. Isosurface plot of the gap size as a function of L, c, and r for a direct structure, square spiral photonic crystal. The isosurface corresponds to a gap size of 10%. The gap is larger than 10% inside the two ''islands.'' The island centered at $L=0.70$ corresponds to [001]-diamond:1 and the one centered at $L=1.65$ corresponds to [001]-diamond:5.

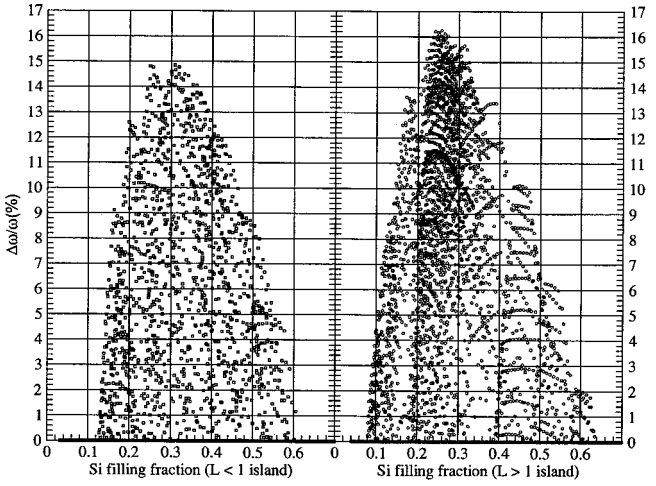

FIG. 7. Gap size as a function of the spirals volume filling fraction for the circular cross section [001]-diamond:1 ($L<1$ island) and [001]-diamond:5 ($L>1$ island) crystals. It is assumed that the solid material has a dielectric constant of 11.9, corresponding to Si.

The orientation of the spirals in the [001]-diamond:1 and [001]-diamond:5 crystals is the same and we choose length L to distinguish between these two types of crystals. Spirals with $L<1$ belong to class [001]-diamond:1 and spirals with $1\leqslant L<2$ belong to class [001]-diamond:5 (see Fig. 2). The crystals of type [001]-diamond:3 are clearly distinguished by the orientation of the spirals relative to the substrate.

A. Direct structure

We consider a direct structure crystal with $\epsilon_b=1$ and $\epsilon_{sp}=11.9$, where the high dielectric component corresponds to Si at wavelengths larger than 2 μm [29]. In order to obtain the photonic band structure, we use a plane waves expansion method [6] with more than 1400 plane waves. The Fourier coefficients of the dielectric are calculated by fast Fourier transform with a sampling of 512^3 points in one unit cell.

In the case of spirals with circular cross-section arms the crystal is completely characterized by L, c, and r. Figure 6 shows an overview of the parameter space sampled in our calculations together with isosurfaces corresponding to parameters for which the relative size of the full photonic band gap is 10%. The parameter space sampled is large enough to contain both the [001]-diamond:1 and [001]-diamond:5 families of crystals. The photonic band gap is larger than 10% in the interior of the two isosurfaces and reaches a local maximum of 14.8% at $[L,c,r]=[0.70,1.35,0.20]$ (first island) and 16.2% at $[L,c,r]=[1.65,1.30,0.13]$ (second island). The GLAD growth angles (see Fig. 1) corresponding to the two optimized structures are 64° and 79°, respectively. The growth angles for the optimized structures above are close to the limits of the current GLAD technology. However, Fig. 6 shows that the size of the PBG is much less sensitive to the pitch of the spirals, c, than the other two parameters, L and r. A spiral photonic crystal in which the spiral arms precisely connect the nearest-neighbor points of the parent, diamond lattice corresponds to $[L,c]=[1/2,\sqrt{2}]$. If the arms precisely connect fifth nearest-neighbor points of diamond, this corresponds to $[L,c]=[3/2,\sqrt{2}]$.

It is also of interest to describe the size of the PBG in relation to the overall volume filling fraction of solid material. In the case of a solid material with the dielectric constant of 11.9, corresponding to Si, we find a sizable gap for a wide range of filling factors of the spiral component, f_{spiral}. Figure 7 shows the relative size of the full PBG for a random sampling of different photonic crystals within a given family. For each of the two islands the relative size of the full PBG is plotted against the Si filling fraction where each point corresponds to a particular $[L,c,r]$ triplet. For [001]-diamond:1 crystals, the envelope of the distribution has a peak at $f_{\text{spiral}}\approx 0.30$ while for the [001]-diamond:5 crystals the distribution peaks at $f_{\text{spiral}}\approx 0.25$.

As an illustrative example in Fig. 8 we show the photonic band structure for the optimized [001]-diamond:5 crystal characterized by $[L,c,r]=[1.65,1.30,0.13]$. The positions of the high symmetry points of the tetragonal Brillouin zone are illustrated in the inset. The frequency in Fig. 8 is measured in units of $a/\lambda_{\text{vac}}=\omega a/2\pi c$ where λ_{vac} is the wavelength in vacuum. A large photonic band gap of relative width 16.2% opens between fourth and fifth bands of the tetragonal band structure. The upper edge of the photonic band gap closes at R point and only two bands (the fifth and sixth) contribute to the spectrum around the upper edge. These lead to an even larger pseudogap of roughly 25% of the center frequency (see Fig. 11).

The spatial distribution of the electromagnetic field in the photonic crystals is also of great interest. The ability to alter the coupling between the matter and radiation field in the photonic crystal is influenced dramatically by the electric field at the specific location [30]. The fourth band in the electromagnetic dispersion relation, for the direct structure described in Fig. 8, exhibits the property of a ''dielectric band.'' In particular the electromagnetic energy near the lower edge of the PBG (upper edge of band 4) is concen-

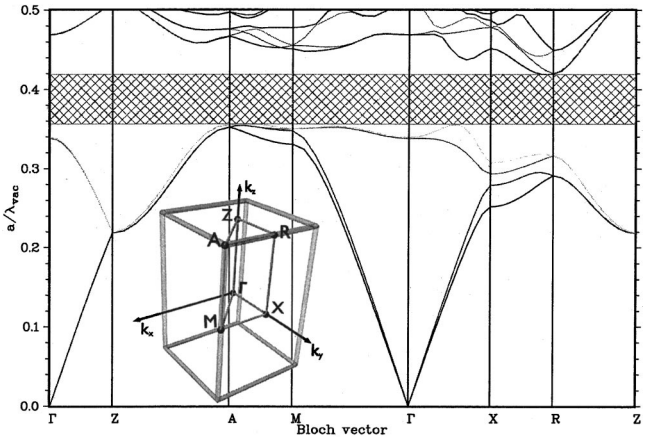

FIG. 8. Band structure for the optimized [001]-diamond:5 square spiral crystal, with arms of circular cross section, characterized by $[L,c,r,]=[1.65,1.30,0.13]$ and $f_{\text{spiral}}=26\%$. The lengths are given in units of a, the lattice constant. The PBG (hashed area) is centered at $a/\lambda_{\text{vac}}=0.39$ and has a width of 16.2% relative to the center frequency. The dielectric constant of the spirals is $\epsilon_{\text{sp}}=11.9$. The inset illustrates the position of the symmetry points of the tetragonal Brillouin zone.

trated primarily in the high dielectric spiral posts. Accordingly, modes near the lower edge of the PBG may be relevant for strong coupling of light in and out of active devices embedded in the solid fraction of the material.

A photonic crystal with connected air component whose structure exhibits ''lines of sight'' can also be used as a device for atom cooling and trapping [31]. As shown in Fig. 4, the square spiral crystals clearly exhibit this property. In Fig. 9 we show the isosurface of $|\vec{E}|$ together with a semitransparent sketch of the spiral for the mode corresponding to the fifth band at the R point (see Fig. 8). In this case, the electromagnetic field intensity is concentrated in the void (air) fraction of the material and very little light enters the higher refractive index (solid) fraction. The field intensity reaches its peak value near the centers of the shaded regions in Fig. 9. These peak intensity regions in the void fraction may act as dipolar optical traps for atomic vapors. The fields in these regions may also exhibit considerable polarization gradients, thereby facilitating the cooling of atoms to very low temperatures. Since the dipolar optical potential created by a single electromagnetic mode exhibits strong periodic modulation on all three spatial dimensions, it may also provide a novel environment for Bose-Einstein condensation of atoms in the void regions of a PBG material. As an example of a dielectric mode we show in Fig. 10 a similar plot for the mode corresponding to fourth band at A point. In this case, the peak intensity regions occur in the dielectric fraction of the material and are preferentially concentrated at the elbows of the square spirals.

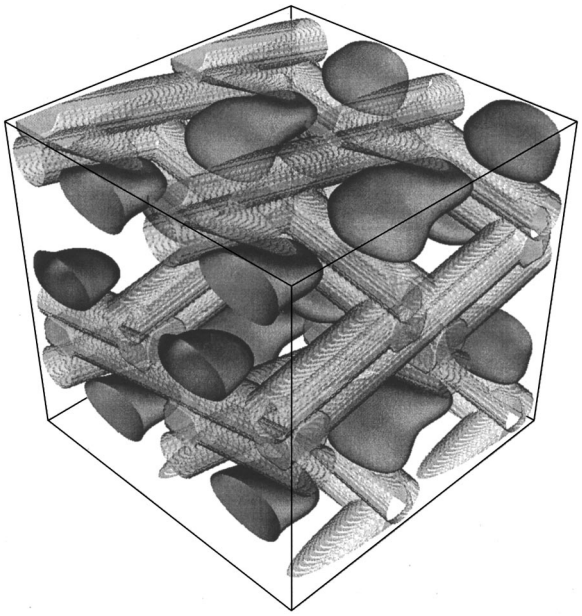

FIG. 9. Absolute value of the electric field for the mode corresponding to the fifth band at R point (see Fig. 8). $|\vec{E}|$ is greater than a certain threshold inside the shaded regions. The shape enclosed by the isosurface is localized in the air component of the crystal.

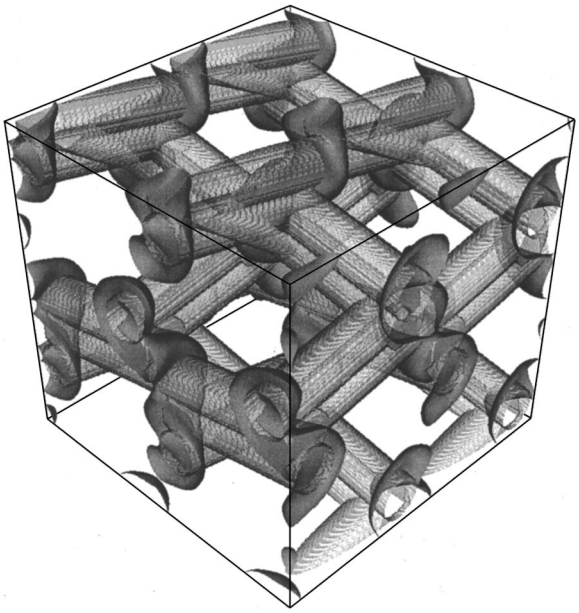

FIG. 10. Absolute value of the electric field for the mode corresponding to the fourth band at A point (see Fig. 8). $|\vec{E}|$ is greater than a certain threshold inside the shaded regions. The shape enclosed by the isosurface is localized mostly in the solid component of the crystal, near the elbows of the spirals.

Figure 8 shows that the lower edge of the photonic band gap falls somewhere on the Γ-X segment, inside the tetragonal Brillouin zone (see Sec. VI for an explanation). This is characteristic for the photonic band structure of many square spiral crystals studied in this paper. However, definitive confirmation of the gap size requires sampling of points throughout the interior and surface of the Brillouin zone. This leads to the calculation of the total electromagnetic density of states (DOS). We find that the maximum error between the gap size as calculated using an extended path on the surface of the Brillouin zone (Γ-M-X-Γ-M-A-Γ-X-R-Γ-A-Z-Γ-R-Z-Γ-A-R-Γ, see the inset of Fig. 8) and the gap size as determined from a total DOS calculation does not exceed a

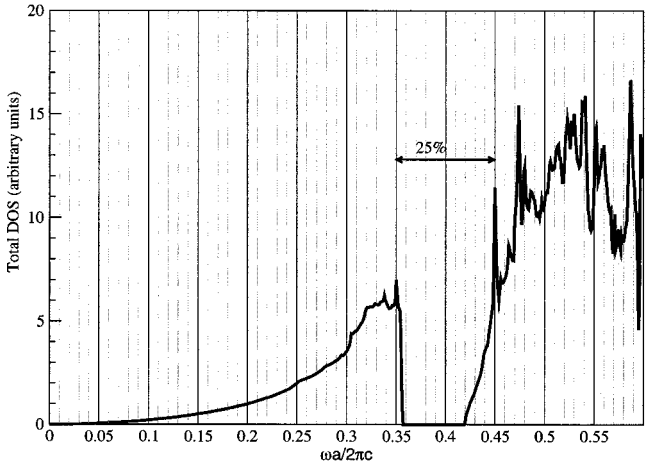

FIG. 11. Total density of states (measured in arbitrary units) for the circular cross section optimized [001]-diamond:5 crystal characterized by $[L,c,r]=[1.65,1.30,0.13]$. The lengths are given in units of a, the lattice constant. The gap has a relative size of 16% and is centered at $a/\lambda_{vac}=0.39$. A pseudogap of 25% opens in this case.

few percents in all the cases tested. The mapping of the gap size as a function of the crystal geometry has been done using the Brillouin zone path mentioned above. However, for all the optimized structures we also provide a total DOS calculation.

In Fig. 11 we show the total density of states for the [001]-diamond:5 crystal whose band structure is shown in Fig. 8. In our calculation we used the improved tetrahedron method [32] adapted to the photonic case. Figure 12 shows the total DOS for the optimized [001]-diamond:1 crystal characterized by $[L,c,r]=[0.70,1.35,0.20]$.

In Fig. 13 the relative size of the full photonic band gap of a direct circular cross section square spirals crystal is plotted as a function of the index contrast. The index contrast is

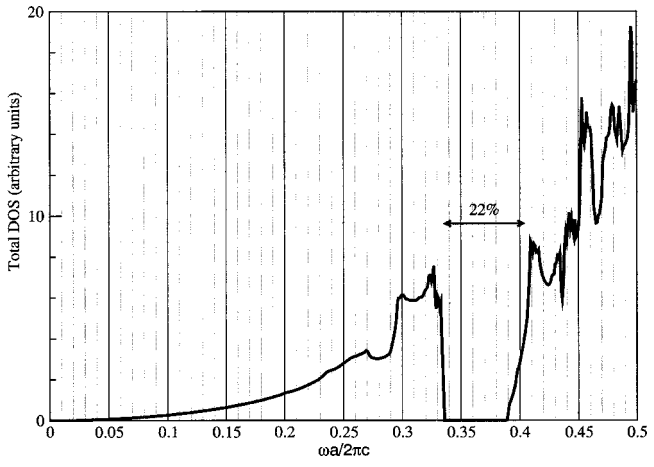

FIG. 12. Total density of states (measured in arbitrary units) for the circular cross section optimized [001]-diamond:1 crystal characterized by $[L,c,r]=[0.70,1.35,0.20]$. The lengths are given in units of a, the lattice constant. The spirals filling fraction in this case is $f_{spiral}=31\%$. The gap is centered at $a/\lambda_{vac}=0.36$ and has a relative size of 14.8%.

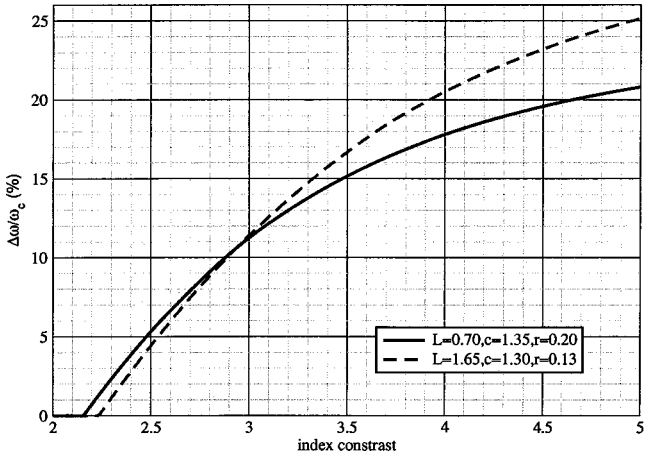

FIG. 13. Relative size of the full photonic band gap as a function of the index contrast for both optimized [001]-diamond:1 and [001]-diamond:5 crystals with circular cross section.

defined as n_{sp}/n_b in this case, where $n_b=\sqrt{\epsilon_b}$ and $n_{sp}=\sqrt{\epsilon_{sp}}$. The two curves correspond to the two optimized geometries: $[L,c,r]=[0.70,1.35,0.20]$ for [001]-diamond:1 (island 1) and $[L,c,r]=[1.65,1.30,0.13]$ for [001]-diamond:5 (island 2) respectively. The threshold for emergence of a complete PBG in the first island is $n_{sp}/n_b=2.15$ whereas for the second island it is $n_{sp}/n_b=2.25$.

From a practical point of view, it is also important to examine the robustness and sensitivity of the PBG to small changes in the geometry of the spirals. For example in the microfabrication process, it is likely that small random variations in the parameters L, c, and r will occur from point to point within the photonic crystal as well as within a single spiral coil. The actual PBG in a weakly disordered photonic crystal will then be given by the intersection of the various PBG's obtained from the set of perfect photonic crystals which sample the distribution of parameters L, c, and r. Figure 14 shows the change in the position of the band edges as

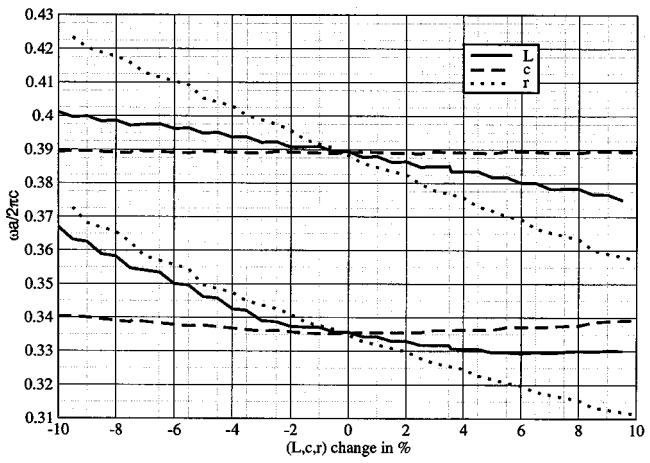

FIG. 14. The band edges as a function of change in the geometry of the spirals. The relative change in L, c, and r are measured in %. The initial geometry was the one corresponding to the optimized [001]-diamond:1 crystal, $[L,c,r]=[0.70,1.35,0.20]$ where the lengths are measured in units of a, the lattice constant.

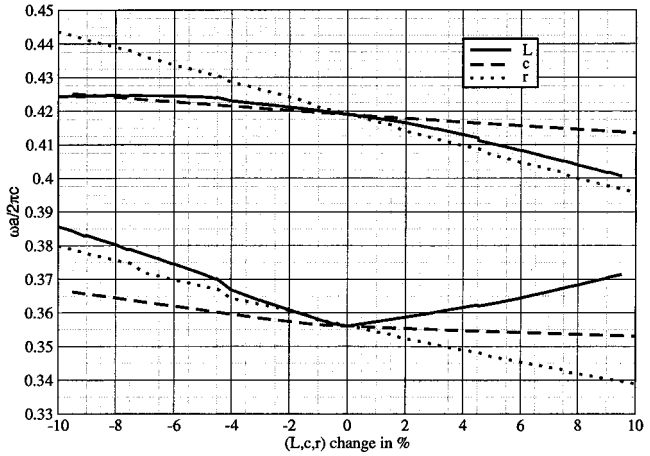

FIG. 15. The band edges as a function of change in the geometry of the spirals. The relative change in L, c, and r are measured in %. The initial geometry was the one corresponding to the optimized [001]-diamond:5 crystal, $[L,c,r]=[1.65,1.30,0.13]$ where the lengths are measured in units of a, the lattice constant.

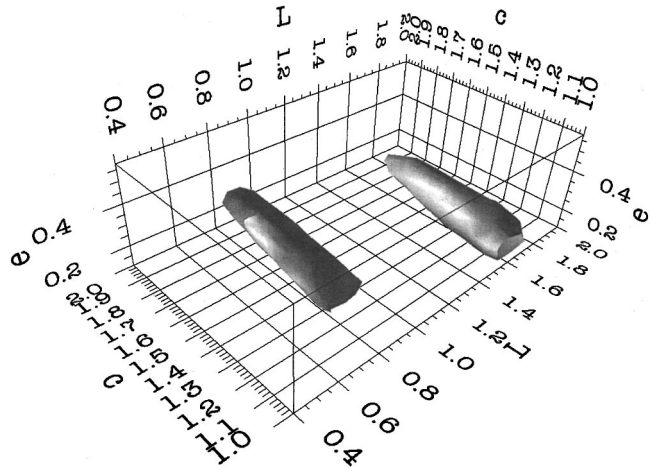

FIG. 16. Isosurface plot of the gap size as a function of L, c, and e for the direct structure, square spiral photonic crystal with arms of square cross section. The isosurface corresponds to a gap size of 10%. The gap is larger than 10% inside the two ''islands.'' The island centered at $L=0.75$ corresponds to [001]-diamond:1 and the one centered at $L=1.65$ corresponds to [001]-diamond:5.

a function of the change in L, c, and r. The frequencies of the band edges are plotted against the relative change in the above parameters. The initial structure (corresponding to change 0%) corresponds to the optimized [001]-diamond:1 crystal and is characterized by $[L,c,r]=[0.70,1.35,0.20]$. Figure 15 shows a similar plot for the optimized [001]-diamond:5 crystal. The jagged character of the curves in these plots is due to the fact that, in the nearly optimized crystal structure, the band edge position is determined by the bands of more than one single k point in the reciprocal space. As the geometry of the spiral is varied around the optimum structure the edge of the photonic band gap jumps discontinuously from one k point to another. Accordingly, the rate of change in the frequency of the band edge with the geometry is only piecewise continuous.

In the analysis presented above, we considered only square spirals crystals whose spiral arms have a circular cross section. In practice, the GLAD microfabrication method can grow arms with noncircular cross section. Depending on the shape of the seed posts, this cross section could be square or rectangular. Here we investigate the effect of such modifications on the photonic band gap. We start with square cross sections. The geometry of the spirals is again described by Fig. 5 where the arm cross section is depicted in Fig. 5(d). In order to completely specify the shape of the square spiral, we require that one of the edges of the square cross section is always parallel to the xy plane. The edges of the square have length e and are measured in units of a, the lattice constant. The crystal is then completely characterized by L, c, and e.

The two PBG islands obtained for the circular-cross-section spirals are present for the square cross section as well. Figure 16 shows an overview of the parameter space sampled in our calculations together with isosurfaces corresponding to parameters for which the relative size of the full photonic band gap is 10%. The parameter space is again large enough and contains both the [001]-diamond:1 and [001]-diamond:5 class of crystals. The photonic band gap is larger than 10% in the interior of the two isosurfaces and reaches a local maximum of 15.0% at $[L,c,e]=[0.75,1.43,0.35]$ (first island) and 15.4% at $[L,c,e]=[1.65,1.25,0.225]$ (second island). The GLAD growth angles corresponding to the two optimized structures are 64° and 79° respectively. In this case we also find that the gap size is less sensitive to the pitch of the spirals, c, than the other two parameters, L and e.

Figure 17 shows the photonic band structure for the optimized square cross section [001]-diamond:5 crystal characterized by $[L,c,e]=[1.65,1.25,0.225]$. The positions of the high symmetry points are shown in the inset of Fig. 8. The frequency in Fig. 17 is measured in units of a/λ_{vac} where

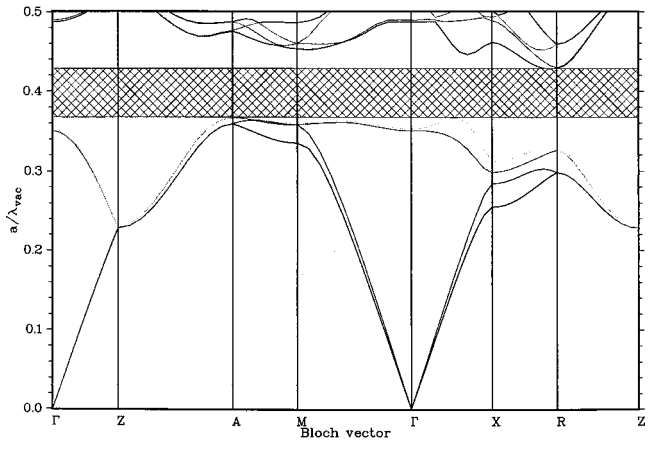

FIG. 17. Band structure for the square cross section optimized [001]-diamond:5 crystal characterized by $[L,c,e]=[1.65,1.25,0.225]$ and $f_{spiral}=24.9\%$. The lengths are given in units of a, the lattice constant. The PBG (hashed area) is centered at $a/\lambda_{vac}=0.40$ and has a width of 15.4% relative to the center frequency. The positions of high symmetry points are illustrated in the inset of Fig. 8. The dielectric constant of the spirals is $\epsilon_{sp}=11.9$.

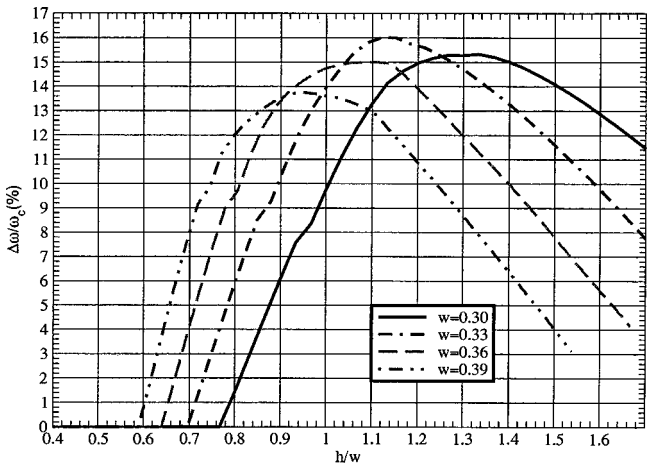

FIG. 18. The relative size of the full PBG as a function of the cross section aspect ratio. The aspect ratio is defined as h/w [see Fig. 5(e)]. The crystal is characterized by $L=0.75$ and $c=1.43$. The dielectric constant of the spirals is $\epsilon_{sp}=11.9$.

λ_{vac} is the wavelength in vacuum. A large photonic band gap of relative width 15.4% opens between fourth and fifth bands. Because the change of the cross section did not affect noticeably the structure of the photonic band structure (compare Figs. 17 and 8) we choose not to show the band structure or the DOS plot for the optimized square cross section [001]-diamond:1 characterized by $[L,c,e]=[0.75,1.43,0.35]$. The PBG of this photonic crystal is centered at $a/\lambda_{vac}=0.365$ and has a relative size of 15.0%.

When the cross section of the spiral arms is rectangular the crystal is characterized by four parameters, L, c and w, h. The geometry of the spirals is again described in Fig. 5, with the arm cross section given in Fig. 5(e). The edge of the rectangle marked with w (its width) in Fig. 5(e) is always parallel to the xy plane. Figure 18 shows the variation of the relative size of the photonic band gap of a rectangular cross section [001]-diamond:1 crystal with the aspect ratio, h/w of the cross section. In Fig. 18 aspect ratio 1 corresponds to the previously studied square cross section. As can be seen, a slight increase of the size of the PBG can be achieved by deforming the spiral arm cross section from a square to a rectangle.

Similar calculations to those described above have been performed for the [001]-diamond:3 family of square spiral photonic crystals derived from third nearest-neighbor points of diamond. The difference between this crystal structure and the ones corresponding to $n=1$ and 5 cases studied above consists in the orientation of the square spiral post relative to the substrate (see Fig. 2). The maximum gap obtained in this case is not as big as the ones obtained previously. The optimized [001]-diamond:3 crystal has a f_{spiral} of 40% and corresponds to $[L,c,r]=[0.81,1.45,0.23]$ where the lengths are measured in units of a. The gap is centered at $a/\lambda_{vac}=0.33$ and has a relative size of 5.8%. Figure 19 shows the important section of the photonic band structure for the optimized [001]-diamond:3 crystal.

B. Inverse structure

Considerably larger photonic band gaps can be obtained by inverting the structures discussed in Sec. IV A. Inverse

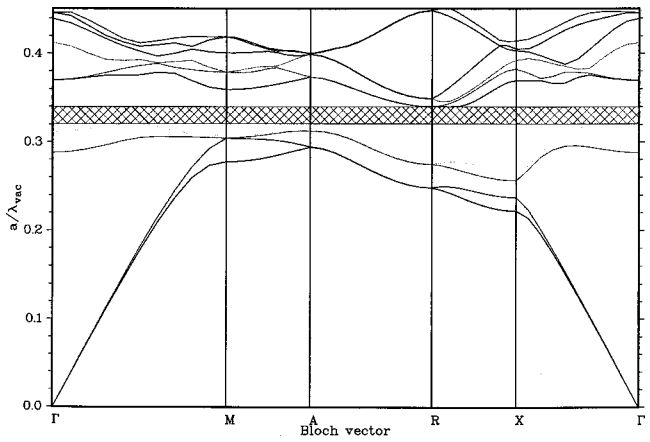

FIG. 19. Band structure for the circular cross section optimized [001]-diamond:3 crystal characterized by $[L,c,r]=[0.81,1.45,0.23]$ and $f_{spiral}=40\%$. The lengths are given in units of a, the lattice constant. The PBG (hashed area) is centered at $a/\lambda_{vac}=0.33$ and has a width of 5.8% relative to the center frequency. The positions of high symmetry points are illustrated in the inset of Fig. 8. The dielectric constant of the spirals is $\epsilon_{sp}=11.9$.

structures can be created in a three stage process. In the first stage a silica based template is created using GLAD. As we will see below the required air filling fraction for an optimized inverted structure is around 80% which implies a significant overlap between adjacent spirals in the template. The overlapping structure can be achieved in stage two by immersing the template from stage one into a liquid solution where further silica growth (increase in the cross-sectional radius of the spiral arms) can be achieved using a sol-gel process [18,33]. In stage three the new template is infiltrated with silicon using chemical vapor deposition and the original silica template is removed by a selective chemical etching process [18]. The inverse structures studied in this section are characterized by $\epsilon_b=11.9$, $\epsilon_{sp}=1$ where the high dielectric component corresponds to Si at wavelengths larger than 2 μm [29]. The methods used for characterization are identical to the ones used in Sec. IV A.

Here, as before, we sample a region of the $[L,c,r]$ parameter space large enough to capture two PBG islands. Figure 20 shows isosurfaces corresponding to parameters for which the relative size of the full photonic band gap is 10%. In other words, the PBG is larger than 10% in the interior of the two isosurfaces. The island centered near $L=0.5$ corresponds to inverse-[001]-diamond:1 family of crystals and the one centered around $L=1.5$ corresponds to the inverse-[001]-diamond:5 family. The optimized inverse-[001]-diamond:1 crystal is characterized by $[L,c,r]=[0.45,1.43,0.395]$ (air filling fraction 81%) and has a full PBG of 22.3% relative size. The optimized inverse-[001]-diamond:5 crystal is characterized by $[L,c,r]=[1.5,1.69,0.333]$ (air filling fraction of 80%) and has a full photonic band gap of 23.6% relative size. The GLAD growth angles corresponding to the two optimized structures are 52° and 74°, respectively. In the case of very large growth angles such as 74°, it may be useful to create the template in three stages rather than two. In this case, stage 2 could be a mechanical compression of the square spiral posts along the z

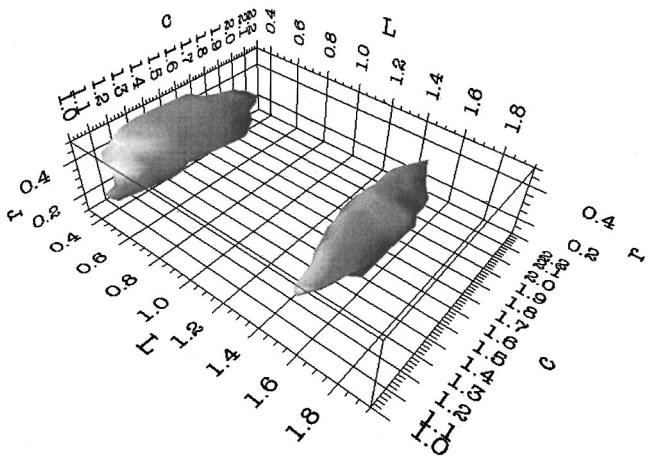

FIG. 20. Isosurface plot of the gap size as a function of L, c, and r for an inverse structure, square spiral photonic crystal with arms of circular cross section. The isosurface corresponds to a gap size of 10%. The gap is larger than 10% inside the two ''islands.'' The island centered at $L=0.45$ corresponds to inverse-[001]-diamond:1 and the one centered at $L=1.5$ corresponds to inverse-[001]-diamond:5.

direction, immediately after their growth by GLAD so as to increase the angle that the arm segments make with respect to the z axis [28].

The band structure for the optimized inverse-[001]-diamond:1 crystal characterized by $[L,c,r]=[0.45,1.43,0.395]$ is shown in Fig. 21.

In Fig. 22 we show the total density of states for the optimized inverse-[001]-diamond:5 crystal characterized by $[L,c,r]=[1.5,1.69,0.333]$.

In Fig. 23 the relative size of the full photonic band gap of a inverse circular cross section square spirals crystal is plotted as a function of the index contrast, n_b/n_{sp}. Here $n_b=\sqrt{\epsilon_b}$ and $n_{sp}=\sqrt{\epsilon_{sp}}$. The two curves correspond to the two optimized geometries: $[L,c,r]=[0.45,1.43,0.395]$ and

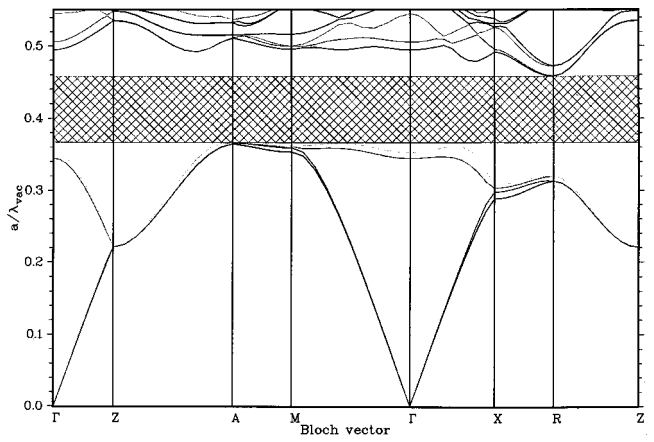

FIG. 21. Band structure for the optimized inverse-[001]-diamond:1 crystal characterized by $[L,c,r]=[0.45,1.43,0.395]$ and $f_{spiral}=81\%$. The lengths are given in units of a, the lattice constant. The PBG (hashed area) is centered at $a/\lambda_{vac}=0.41$ and has a width of 22.3% relative to the center frequency. The positions of high symmetry points are illustrated in the inset of Fig. 8.

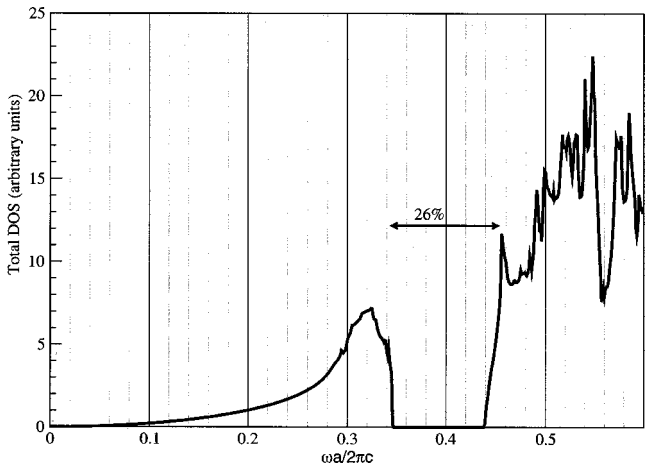

FIG. 22. Total density of states (measured in arbitrary units) for the circular cross section optimized inverse-[001]-diamond:5 crystal characterized by $[L,c,r]=[1.50,1.69,0.333]$ and $f_{spiral}=80\%$. The lengths are given in units of a. The gap is centered at $a/\lambda_{vac}=0.39$ and has a relative size of 23.6%.

$[L,c,r]=[1.50,1.69,0.333]$. The threshold for the first island is $n_b/n_{sp}=2.15$ whereas for the second island it is $n_b/n_{sp}=2.25$.

The circular arm cross section of the inverse structures is quite important for the creation of a very large PBG. For comparison, we consider inverse-[001]-diamond:n crystals whose arms have a square cross section. The crystal is completely characterized by the parameters L, c, and e [see Fig. 5(d)]. The two PBG islands in parameter space found previously for the (direct) [001]-diamond:n crystals are found in this case also. In Fig. 24 we show the band structure of the optimized inverse-[001]-diamond:1 characterized by $[L,c,e]=[0.57,1.20,0.57]$ and in Fig. 25 we show the band structure of the optimized inverse-[001]-diamond:5 characterized by $[L,c,e]=[1.50,1.75,0.575]$. The optimum PBG's are now 15.4% and 16.6%, respectively. While these gaps are moderately large, they are noticeably smaller than those

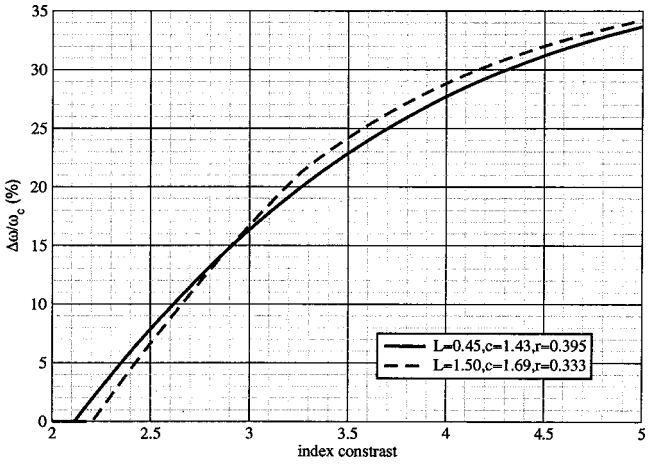

FIG. 23. Relative size of the full photonic band gap as a function of the index contrast for both optimized inverse-[001]-diamond:1 and inverse-[001]-diamond:5 crystals with circular cross section.

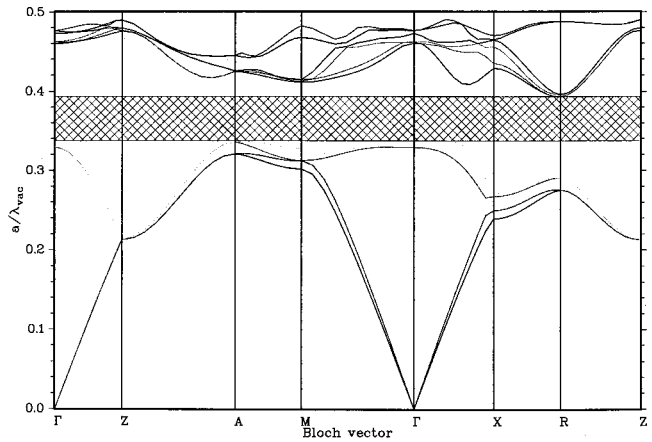

FIG. 24. Band structure for the square cross section optimized inverse-[001]-diamond:1 crystal characterized by $[L,c,e]=[0.57,1.20,0.57]$ and $f_{\text{spiral}}=66.7\%$. The lengths are given in units of *a*, the lattice constant. The PBG (hashed area) is centered at $a/\lambda_{\text{vac}}=0.36$ and has a width of 15.4% relative to the center frequency. The positions of high symmetry points are illustrated in the inset of Fig. 8. The dielectric constant of the background is $\epsilon_{\text{b}}=11.9$.

of the optimized inverse square spiral structures with circular arm cross sections.

We note, finally, that the inverse-[001]-diamond:3 crystal structures do not provide a large PBG. The optimized crystal structure corresponds to $[L,c,r]=[1.52,1.31,0.25]$ and has a gap of 4.9% opening between bands 4 and 5 of the tetragonal band structure. The gap is centered at $a/\lambda_{\text{vac}}=0.42$ and $f_{\text{spiral}}=79\%$.

V. [001]-FCC:*n* STRUCTURES

It is evident from the examples of the preceding section that square spiral structures with the appropriate geometry

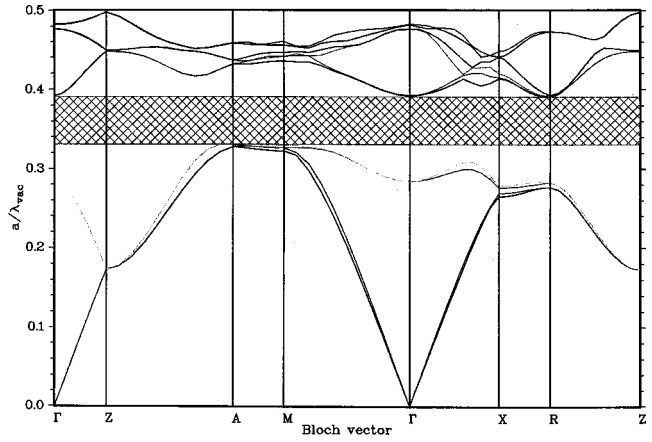

FIG. 25. Band structure for the square cross section optimized inverse-[001]-diamond:5 crystal characterized by $[L,c,e]=[1.50,1.75,0.575]$ and $f_{\text{spiral}}=74.6\%$. The lengths are given in units of *a*, the lattice constant. The PBG (hashed area) is centered at $a/\lambda_{\text{vac}}=0.36$ and has a width of 16.6% relative to the center frequency. The positions of high symmetry points are illustrated in the inset of Fig. 8. The dielectric constant of the background is $\epsilon_{\text{b}}=11.9$.

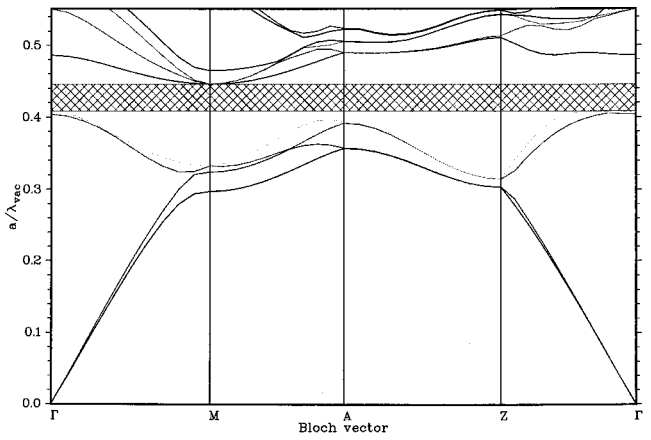

FIG. 26. Band structure for the circular cross section optimized [001]-FCC:1 crystal characterized by $[L,c,r]=[0.75,0.83,0.17]$ and $f_{\text{spiral}}=33.5\%$. The lengths are given in units of *a*, the lattice constant. The PBG (hashed area) is centered at $a/\lambda_{\text{vac}}=0.43$ and has a width of 8.8% relative to the center frequency. The positions of high symmetry points are illustrated in the inset of Fig. 8. The dielectric constant of the spirals is $\epsilon_{\text{sp}}=11.9$.

can exhibit photonic band gaps that rival the optimized tetrahedrally bonded (diamond) network. While it is tempting to associate these large gaps with the presence of a diamond parent lattice, we emphasize that the optimized square spiral structure deviates from the original parent lattice. It is also apparent that the specific choice of the bonding arms is crucial to PBG formation. The fact that the structures in the [001]-diamond:3 family do not provide a large PBG demonstrates that not all bonding networks within a given lattice are equally effective. Indeed the fifth nearest-neighbor spiral structure is more effective than the one related to nearest-neighbor diamond bonds. In this section we show that certain parent lattices that are not traditionally associated with large photonic band gaps, can exhibit large gaps with appropriate optimization of square spiral arms. To this end, we consider photonic crystals from the [001]-FCC:*n* family. While previously studied FCC lattices exhibit only pseudo-gaps between low-order bands in the electromagnetic dispersion, we show that relatively large, fundamental PBG's can be created from the FCC lattices employing the square spiral post architecture. In particular, for an optimized inverse structure (air posts in a silicon background), the FCC lattice yields a PBG as large as 17%.

The square spiral crystal in the FCC case is similar to the one studied in Sec. IV. The building block of the crystal is described in Fig. 5. The substrate is again a square lattice of lattice constant *a* as shown in Fig. 1(a). The only difference between these crystals and the ones studied previously is the orientation of the spirals relative to the substrate [see Fig. 4(c)]. As shown in Fig. 3 the spirals of the [001]-FCC:1 and [001]-FCC:5 structures are rotated by 45° relative to the square lattice of seed posts on the substrate (and to their diamond counterparts).

Figure 26 shows the relevant section of the photonic band structure for the optimized [001]-FCC:1 crystal characterized by $[L,c,r]=[0.75,0.83,0.17]$ and $f_{\text{spiral}}=33.5\%$. The gap opens between bands 4 and 5 of the tetragonal band struc-

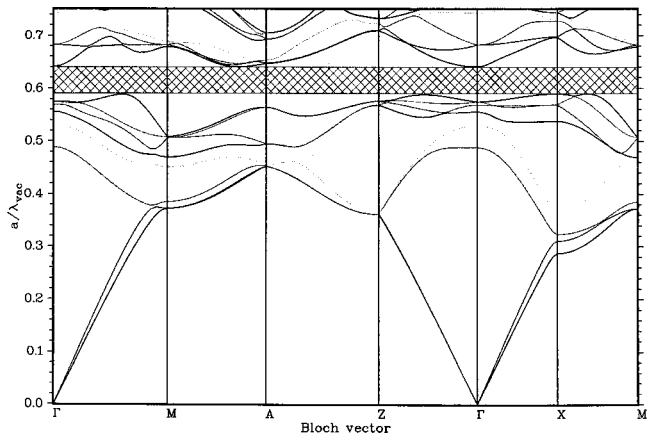

FIG. 27. Band structure for the circular cross section optimized [001]-FCC:5 crystal characterized by $[L,c,r]=[1.23,0.81,0.11]$ and $f_{\text{spiral}}=23.2\%$. The lengths are given in units of a, the lattice constant. The PBG (hashed area) is centered at $a/\lambda_{\text{vac}}=0.61$ and has a width of 8.3% relative to the center frequency. The positions of high symmetry points are illustrated in the inset of Fig. 8. The dielectric constant of the spirals is $\epsilon_{\text{sp}}=11.9$.

ture, has a relative size of 8.8% and is centered at $a/\lambda_{\text{vac}}=0.43$. For the [001]-FCC:5 family we find a sizable gap opening between bands 8 and 9 of the tetragonal band structure. Figure 27 shows the relevant section of the photonic band structure for the optimized [001]-FCC:5 crystal characterized by $[L,c,r]=[1.23,0.81,0.11]$ and $f_{\text{spiral}}=23.2\%$. While for the optimized [001]-FCC:5 crystal the full PBG opens between bands 8 and 9, for other sets of parameters (in the [001]-FCC:5 family) we find a modest bandgap opening between bands 4 and 5.

Figure 28 shows the photonic band structure for the optimized inverse-[001]-FCC:1 crystal characterized by $[L,c,r]=[0.67,0.94,0.32]$ and $f_{\text{spiral}}=81.1\%$. The gap in this case is centered at $a/\lambda_{\text{vac}}=0.50$ and has a relative size of 17%. For the optimized inverse-[001]-FCC:5 we find an optimized structure characterized by $[L,c,r]=[1.30,1.22,0.27]$ and $f_{\text{spiral}}=79\%$ whose band gap again opens between bands 4 and 5 of the tetragonal band structure and has a relative size of 10.6%. The gap in this case is centered at $a/\lambda_{\text{vac}}=0.42$.

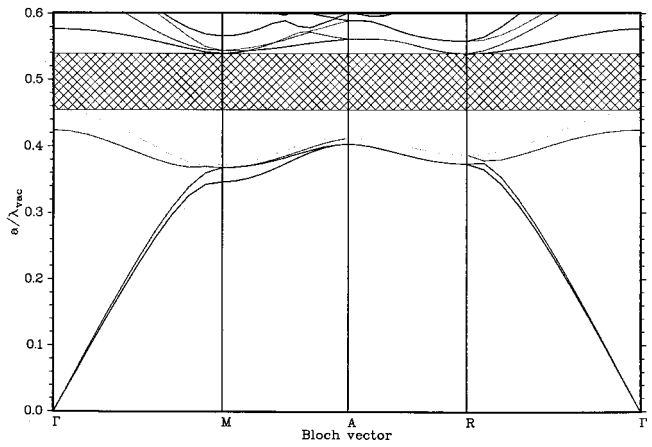

FIG. 28. Band structure for the circular cross section optimized inverse-[001]-FCC:1 crystal characterized by $[L,c,r]=[0.67,0.94,0.32]$ and $f_{\text{spiral}}=81.1\%$. The lengths are given in units of a, the lattice constant. The PBG (hashed area) is centered at $a/\lambda_{\text{vac}}=0.50$ and has a width of 17.0% relative to the center frequency. The positions of high symmetry points are illustrated in the inset of Fig. 8. The dielectric constant of the spirals is $\epsilon_{\text{sp}}=11.9$.

VI. CONNECTION WITH DIAMONDLIKE STRUCTURES

In order to complete our discussion, we provide a direct comparison of our square spiral photonic crystals with other architectures that are traditionally associated with a large 3D photonic band gap. We note in passing that our square spiral architecture appears to provide larger gaps than other polygonal spiral post structures. For instance, we have studied the parameter space of triangular post structures based on the diamond parent lattice as well as distorted diamond parent lattices. Despite the fact that triangular spirals can connect all lattice points of diamondlike lattices, we find only small 3D PBG's in the cases studied. In this section, we compare traditional diamond structures with our recently introduced [001]-diamond:*n* square spirals.

As discussed in Sec. III the elbows of the spirals in our crystals may, in general, be substantially removed from the original points of a pure diamond lattice. However, the elbows of the optimal crystals (for which the PBG is maximal) are in general proximal to the points of a diamond lattice that has undergone a suitable tetragonal distortion. It is also apparent that the square spiral arms lead to a lowering of the overall symmetry of the crystal relative to that of the pure diamond lattice of spheres or the tetrahedral bonding network. Here we compare the band structure of the optimized inverse-[001]-diamond:5 square spiral with those of the two best diamond structures, reported in previous literature, along a common trajectory in wave-vector space. The diamond structure can also be viewed as a tetragonal lattice with a basis of four points. This can be seen easily in Fig. 2 where any of the 1-2-3-4 set of spheres connected by thick lines can be used as a basis on the tetragonal lattice formed by the centers of type 1 spheres. Figure 29(a) shows a general diamond structure consisting of balls on the pure diamond lattice with sticks connecting all nearest-neighbor points. This defines a parameter space consisting of the ball radius r_s and the stick (cylinder) radius r_c. Both direct and inverse diamond network structures are investigated in this parameter space. The structures corresponding to local maxima in the PBG as a function of these parameters are shown in Figs. 29(b) and 29(c). Figure 29(b) shows the tetrahedral bonding optimum in which the cylinder radius exceeds the ball radius. For a direct structure with solid cylinders of dielectric constant 11.9, $r_c=0.1$, $r_s=0$, and overall dielectric volume filling fraction of 17.8%, the PBG is 28.4%. This is a variation of the A7 structure studied previously [7] in which it was assumed that the cylinders had a dielectric constant of 12.96 rather than 11.9. Figure 29(c) shows an inverse diamond structure in which the spheres (made of air) have a large radius (which causes them to overlap significantly) so as to completely engulf the cylinders. The air spheres are

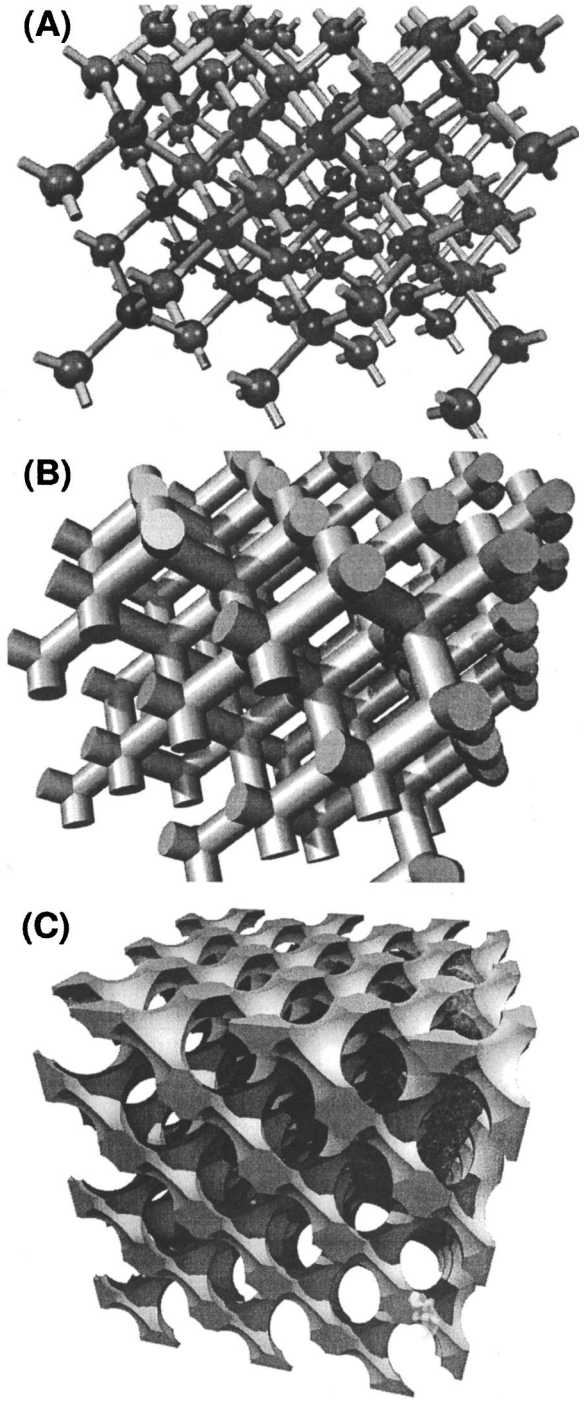

FIG. 29. (a) Ball and stick diamond network crystal is formed by placing spheres on a diamond lattice and joining the first-order neighbors with cylinders. Both the spheres and the cylinders are made from the same material. (b) The optimized tetrahedral bonding network. (c) The optimized inverse diamond.

assumed to be embedded in a background with dielectric constant 11.9. For this inverted diamond structure the maximum gap size is 27.3% and corresponds to an air filling fraction of 81.2%.

For the direct diamond network structure the spheres do not help the formation of the PBG. Figure 30 shows the variation of the full photonic band gap with r_c for a direct

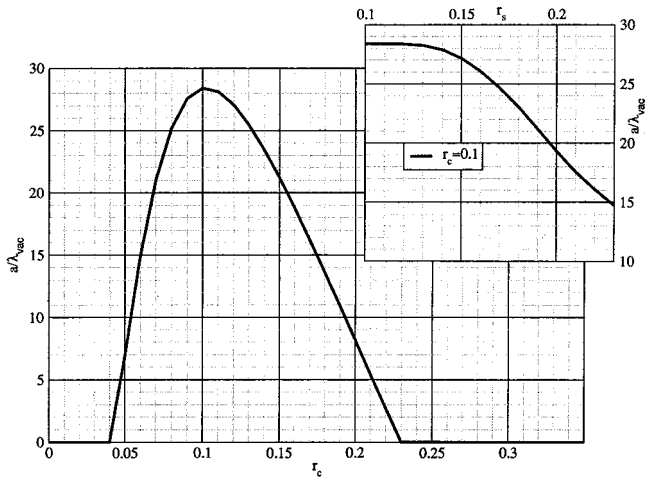

FIG. 30. Relative size of the full photonic band gap as a function of r_c for a direct diamond network crystal made from a material with $\epsilon_{mat}=11.9$ and $r_s=0$. The inset shows the variation of the gap size with r_s for $r_c=0.1$. The optimized crystal has a band gap of relative size 28.4% centered at $a/\lambda_{vac}=0.60$ and is characterized by $r_c=0.1$, $r_s=0$. The lengths are measured in units of a, the FCC lattice constant.

structure made from a material with $\epsilon_{mat}=11.9$. The inset of Fig. 30 shows the variation of the photonic band gap size with r_s for $r_c=0.1$. Spheres with $r_s \leqslant 0.1$ are not visible in this structure because they are fully engulfed by the cylindrical bonds.

Figure 31 shows the tetragonal photonic band structure for (a) the optimized inverse-[001]-diamond:5, (b) the optimized direct diamond network (tetrahedral bonding) and (c) the optimized inverted diamond photonic crystals. In all three cases the crystal is modeled as a basis on a tetragonal lattice of *xy* lattice constant *a*. The *z* lattice constant is $c=a\sqrt{2}$ for the diamond crystals and $c=1.69a$ for the inverse-[001]-diamond:5 crystal. The path in the reciprocal space passes through the important symmetry points of the tetragonal Brillouin zone (see the inset of Fig. 8) and also through the important symmetry points of the FCC Brillouin zone. The symmetry points DU, DL, DX, DW, and DK in Fig. 31 correspond to the symmetry points *U*, *L*, *X*, *W*, and *K*, respectively, of a FCC Brillouin zone of lattice constant $p=a\sqrt{2}$ which is rotated by 45° relative to the tetragonal Brillouin zone. Figure 3 provides a useful visualization of the relative size and orientation of the FCC and tetragonal lattices. The wave-vector path DX-DU-DL-Γ-DX-DW-DK shown in Fig. 31 is the standard path chosen in the FCC Brillouin zone to depict band structure for the diamondlike structures. The only difference is that the number of states for a given Bloch vector is double that of the standard diamond band structure, since we use a unit cell that is twice the volume of the standard FCC primitive cell. The position of the symmetry points in (a) is slightly different from that of (b) and (c) because of the different values of *c* used in the respective cases. The lower part of the band structure (first four bands) is very similar in all three cases, except for the noticeable breaking of the degeneracy along some of segments of the square spiral bands. We note that the Γ-*M*

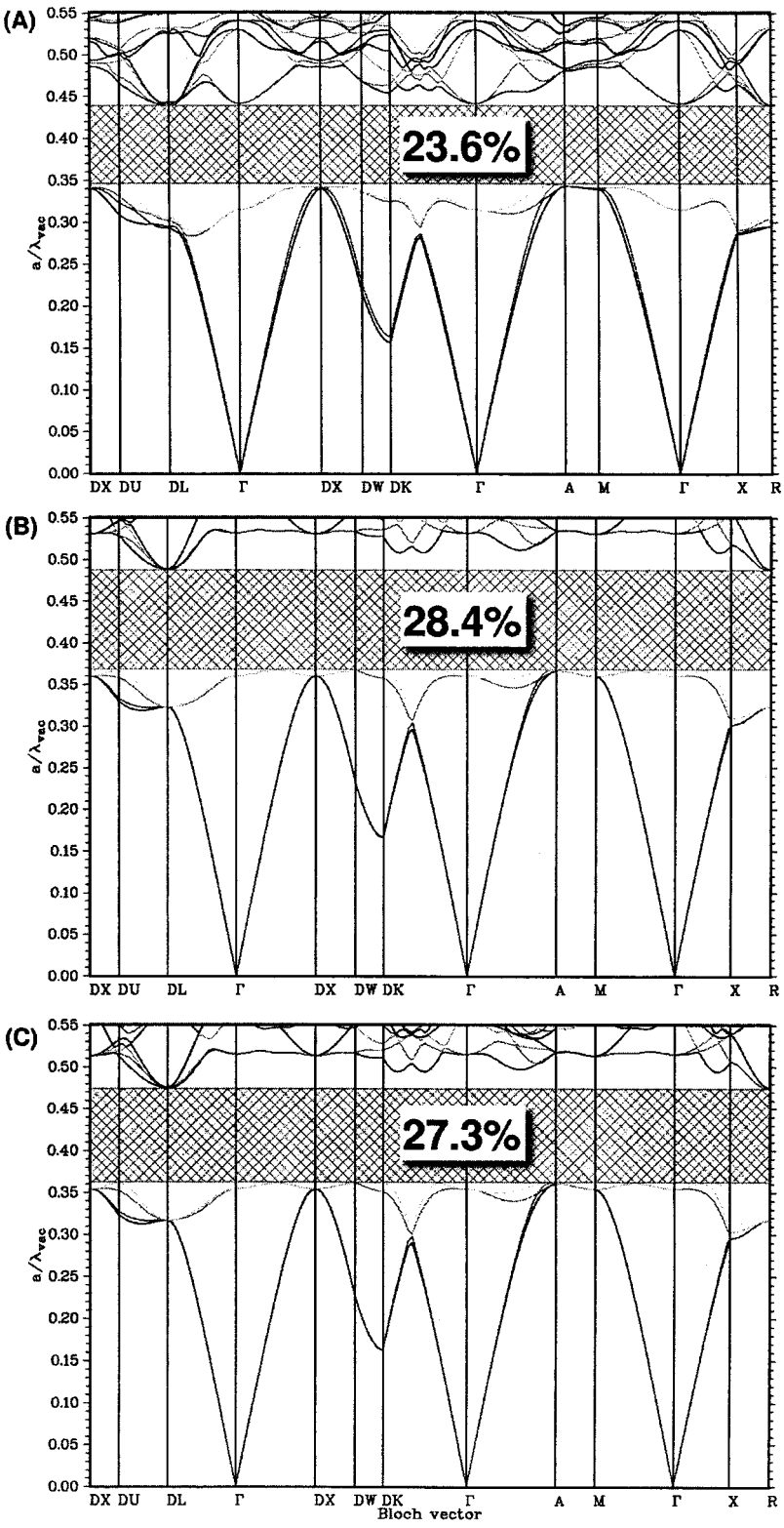

FIG. 31. Tetragonal band structures for the optimized inverse-[001]-diamond:5 (a), optimized diamond (tetrahedral bonding) network (b) and optimized inverted diamond (c) photonic crystals. The dielectric constant of the material used is 11.9. The path in the reciprocal space passes through the relevant symmetry points of the FCC Brillouin zone (these are the points prefixed by D) and then through the relevant symmetry points of the tetragonal Brillouin zone (illustrated in the inset of Fig. 8).

segment of the tetragonal Brillouin zone is identical to the segment Γ-DX of the rotated FCC Brillouin zone. Also the Γ-*X* segment of the tetragonal Brillouin zone lies along the Γ-DK segment of the rotated FCC Brillouin zone.

We mentioned earlier (Sec. IV A) that in some cases the photonic band edge of the square spiral photonic crystal occurs inside (rather than on the surface of) the tetragonal Brillouin zone (see Fig. 8). Figure 31 shows that the bands along the tetragonal Γ-*X* segment can be associated with the bands along the FCC Γ-*K* segment (the folding back of the bands along segment Γ-DK is apparent in Fig. 31). By noting that in the case of the FCC Brillouin zone the extended Γ-*K* path is equivalent to the union of the Γ-*K* and *U*-*X* segments we associate the ''bump'' in the third and fourth bands along the

Γ-X segment with the closing of the lower edge of the diamond band structure along the FCC U-X segment [6].

Figure 31 shows that the primary advantage of the true diamond crystals over the optimized inverse-[001]-diamond:5 crystal in PBG formation comes near the upper band edge. The upper band edge for the square spiral crystal occurs at DL, R (related to DL) and Γ, whereas for the diamond structures, it occurs only at DL and R as seen in Figs. 31(b) and 31(c). We point out, however, that the closing of the upper edge of the PBG at the Γ point is not a characteristic of all square spirals crystals studied in this paper.

VII. CONCLUSIONS

In conclusion, we have shown that tetragonal, square spiral, photonic crystals offer a unique avenue to large scale microfabrication of materials with very large and robust 3D PBG's at near visible wavelengths. Unlike traditional diamond structures which involve complicated microfabrication strategies, the present blueprint can be realized using a relatively straightforward glancing angle deposition (GLAD) method. The distinguishing characteristic of our architecture is most apparent if one considers a sequence of slices of the structure (membranes) normal to the [001] crystallographic direction. Starting from the two-dimensional array of seed posts on the surface of the substrate and moving upward, it is apparent that each subsequent slice arises from a continuous (global) translation of a fixed 2D photonic crystal membrane, consisting of a square lattice of identical shapes. A rotation of the extruded shape is achieved at the elbows of the spiral by a change of direction of vapor flux impinging on the growing sample. This is very different from other 3D photonic crystals. For example, in the diamond crystals depicted in Figs. 29(b) and 29(c) different slices along the [001] direction would yield widely varying 2D photonic crystal membranes. The complexity of 3D microlithography for these cases arises from the variations in the 2D pattern. Even for the well known ''woodpile'' PBG materials [14], 3D microlithography is laborious [14,16]. In this case, the 2D slices (membranes) correspond to simple stripes. However, from one layer to the next layer of the woodpile, this membrane undergoes a large discrete rotation and translation. This discontinuous movement of the membrane from one slice to the next, leads to air gaps directly underneath rods of the woodpile structure, which require masking before growth of the next layer. Such complications do not arise in our blueprint.

Notwithstanding similarities to diamond structures with suitably reduced symmetries, our square spiral PBG material belongs to a relatively unique class of photonic crystals with a large gap between the fourth and fifth photon dispersion bands. This large PBG prevails even when the square spirals are based on the FCC lattice rather than the diamond lattice. Since the PBG of our square spiral architecture is related to the fundamental (lowest possible) gap of diamond in the electromagnetic dispersion, it is highly robust to disorder effects. We find a set of parameters for both the direct and inverted structure for which the relative size of the photonic band gap has a local maximum. The optimized crystal has a large full photonic band gap and a considerably larger pseudogap. We find the gap to be very stable with respect to crystal's geometrical parameters and also relatively insensitive to the transition from a topologically disconnected to a connected high dielectric component.

We believe that square spiral PBG materials are amenable to the incorporation of planar integrated microcircuits for light within the large PBG. These can be engineered within two-dimensional capping layers [26,28] that are embedded (sandwiched) within the square spiral photonic crystal. Such planar defects can be created with relatively minor changes in the deposition algorithm used to create the original square spiral crystal.

ACKNOWLEDGMENTS

We are grateful to Scott Kennedy and Mike Brett for a number of stimulating discussions. This work was supported in part by the Natural Sciences and Engineering Research Council of Canada and a grant from William F. McLean.

[1] Sajeev John, Phys. Rev. Lett. **58**, 2486 (1987).
[2] Eli Yablonovitch, Phys. Rev. Lett. **58**, 2059 (1987).
[3] Sajeev John, Ovidiu Toader, and Kurt Busch, Encyclopedia Phys. Sci. Technol. **12**, 133 (2002).
[4] Sajeev John, Phys. Rev. Lett. **53**, 2169 (1984).
[5] J. D. Joannopoulos, P. R. Villeneuve, and S. Fan, Nature (London) **386**, 143 (1997).
[6] K. M. Ho, C. T. Chan, and C. M. Soukoulis, Phys. Rev. Lett. **65**, 3152 (1990).
[7] C. T. Chan, S. Datta, K. M. Ho, and C. M. Soukoulis, Phys. Rev. B **50**, 1988 (1994).
[8] E. Yablonovitch, T. J. Gmitter, and K. M. Leung, Phys. Rev. Lett. **67**, 2295 (1991).
[9] S. Ottow, V. Lehmann, and H. Föll, Appl. Phys. A: Mater. Sci. Process. **63**, 153 (1996).
[10] M. Christophersen, J. Carstensen, A. Feuerhake, and H. Föll, Mater. Sci. Eng., B **69**, 194 (2000).
[11] K. Wang, A. Chelnokov, S. Rowson, P. Garoche, and J.-M. Lourtioz, J. Phys. D **33**, L119 (2000).
[12] K. M. Ho, C. T. Chan, K. M. Ho, C. M. Soukoulis, R. Biswas, and M. Sigalas, Solid State Commun. **89**, 413 (1994).
[13] H. S. Sozuer and J. P. Dowling, J. Mod. Opt. **41**, 231 (1994).
[14] S. Y. Lin, J. G. Fleming, D. L. Hetherington, B. K. Smith, R. Biswas, K. M. Ho, M. M. Sigalas, W. Zubrzycki, S. R. Kurtz, and Jim Bur, Nature (London) **394**, 251 (1998).
[15] Shawn-Yu Lin and J. G. Fleming, J. Lightwave Technol. **17**, 1944 (1999).
[16] Susumu Noda, Katsuhiro Tomoda, Noritsugu Yamamoto, and Alongkarn Chutinan, Science **289**, 604 (2000).
[17] Younan Xia and George M. Whitesides, Angew. Chem. Int. Ed. Engl. **37**, 550 (1998).
[18] Alvaro Blanco, Emmanuel Chomski, Serguei Grabtchak, Marta Ibisate, Sajeev John, Stephen W. Leonard, Cefe López, Francisco Meseguer, Herman Miguez, Jessica P. Mondia,

Geoffrey A. Ozin, Ovidiu Toader, and Henry M. van Driel, Nature (London) **405**, 437 (2000).
[19] Hernan Miguez, Emmanuel Chomski, Florencio Garcia-Santamaria, Maria Ibisate, Sajeev John, Cefe López, Francisco Meseguer, Jessica P. Mondia, Geoffrey A. Ozin, Ovidiu Toader, and Henry M. van Driel, Adv. Mater. **13**, 1634 (2001).
[20] Yurii A. Vlasov, Xiang-Zheng Bo, James C. Sturm, and David J. Norris, Nature (London) **414**, 289 (2001).
[21] H. Sami Sözüer and Joseph W. Haus, J. Opt. Soc. Am. B **10**, 296 (1993).
[22] Alongkarn Chutinan and Susumu Noda, Phys. Rev. B **57**, 2006 (1998).
[23] K. Robbie and M. J. Brett, Nature (London) **384**, 616 (1996).
[24] Brian H. Cumpston, Sundaravel P. Ananthavel, Stephen Barlow, Daniel L. Dyer, Jeffrey E. Ehrlich, Lael L. Erskine, Ahmed A. Heikal, Stephen M. Kuebler, I.-Y. Sandy Lee, Dianne Mccord-Maughon *et al.*, Nature (London) **398**, 51 (1999).
[25] Ya-Chih Tsai, John B. Pendry, and Kenneth W.-K. Shung, Phys. Rev. B **59**, 10 401 (1999).
[26] K. Robbie and M. J. Brett, J. Vac. Sci. Technol. B **15**, 1460 (1997).
[27] Scott R. Kennedy, Michael J. Brett, Ovidiu Toader, and Sajeev John, Nano Lett. **1**, 59 (2002).
[28] M. W. Seto, K. Robbie, D. Vick, M. J. Brett, and L. Kuhn, J. Vac. Sci. Technol. B **17**, 2172 (1999).
[29] *Handbook of Optical Constants of Solids*, edited by Edward D. Palik (Academic Press Inc., Orlando, 1985).
[30] Kurt Busch and Sajeev John, Phys. Rev. E **58**, 3896 (1998).
[31] Ovidiu Toader, Sajeev John, and Kurt Busch, Opt. Express **8**, 217 (2001).
[32] Peter E. Blochl, O. Jepsen, and O. K. Andersen, Phys. Rev. B **49**, 16 223 (1994).
[33] W. Stober, A. Fink, and E. Bohn, J. Colloid Interface Sci. **26**, 62 (1968).